JGR Space Physics

RESEARCH ARTICLE
10.1029/2025JA034977

Special Collection:
Space Weather Events of 2024 May 9-15

A New Method for Probabilistic Spatiotemporal Forecasts of Solar Soft X-Ray "S-Class" (>X10) Superflares

V. M. Velasco Herrera[1], G. Velasco Herrera[2], W. Soon[3,4], A. Özgüç[5], N. Babynets[6], A. Tlatov[7], M. Švanda[8], S. Qiu[9], S. Baliunas[10], B. Kotan[5], G. González González[11], L. A. Bautista Flores[12], and M. Pazos[13]

[1]Instituto de Geofísica, Universidad Nacional Autónoma de México, Ciudad Universitaria, Ciudad de México, México, [2]Instituto de Ciencias Aplicadas y Tecnología, Universidad Nacional Autónoma de México, Ciudad Universitaria, Ciudad de México, México, [3]Institute of Earth Physics and Space Science (EPSS), Sopron, Hungary, [4]Center for Environmental Research and Earth Sciences, Salem, MA, USA, [5]Kandilli Observatory and Earthquake Research Institute, Istanbul, Turkey, [6]Escuela Nacional de Lenguas, Lingüística y Traducción, Universidad Nacional Autónoma de México, Ciudad Universitaria, Ciudad de México, México, [7]Kislovodsk Mountian Astronomical Station of the Pulkovo Observatory, Kislovodsk, Kalmyk State University, Elista, Russian Federation, [8]Astronomical Institute of the Czech Academy of Sciences, Ondřejov, Czech Republic, [9]Department of Geophysics, College of the Geology Engineering and Geomatics, Chang'an University, Xi'an, China, [10]Retired, Harvard-Smithsonian Center for Astrophysics, Cambridge, MA, USA, [11]Facultad de Ciencias, Universidad Nacional Autónoma de México, Ciudad de México, México, [12]Instituto Politécnico Nacional, Ciudad de México, México, [13]Instituto de Ciencias Atmosféricas y Cambio Climático, Universidad Nacional Autónoma de México, Ciudad de México, México

Abstract Solar superflares of S-class (>X10 in soft X-rays) pose extreme space weather hazards, yet their prediction remains a fundamental challenge owing to their rapid and transient natures and the limitations of conventional event-based forecasts. We introduce for the first time, a probabilistic spatiotemporal framework designed to identify extended epochs and heliographic zones with heightened superflare likelihood, rather than predicting individual events. Our methodology analyzes nearly five decades of Geostationary Operational Environmental Satellites SXR observations (1975–2025) and introduces two novel components: (a) a cross-Laplacian diagnostic, derived from the butterfly diagrams of sunspot area and SXR flare density, which identifies photosphere-corona coupling and pinpoints magnetic energy accumulation sites as preferential zones for S-flare occurrence; and (b) a temporal model based on the coupled phase states of 1.7-year and 7-year oscillations, extracted via wavelet analysis and projected forward using a Bayesian Least-Squares Support Vector Machine method. Integrating these spatial and temporal diagnostics yields a unified forecast, we identify 2025.7–2026.6 and 2027.2–2027.9 years, as the primary high-probability windows for S-class flare activity during Solar Cycle 25, corresponding preferentially to latitudinal bands in the southern (5°S–25°S) and northern (10°N–30°N) hemispheres, respectively. Subsequent windows are projected for Cycle 26. This physics-informed, probabilistic approach provides a robust strategy for anticipating periods of extreme solar activity by characterizing the inherent patterns of magnetic energy storage and release in the solar atmosphere.

Plain Language Summary Solar superflares, the most powerful explosions in our solar system, can cause severe disruptions to space technology and are very dangerous for the lives of astronauts, power grids, and communications systems on Earth. Forecasting these extreme events, including the most recent May 2024 storm event, has been one of the biggest challenges in the frontier of space weather science. In this study, we developed a new approach to forecast these superflares (classified as S-class or ≥X10 class in soft X-rays) by analyzing nearly 50 years of satellite observations. We are proposing a paradigm shift; instead of trying to predict the exact location and time, we identify time windows and heliographic zones where the probability of superflares is significantly enhanced. Our analysis reveals that these extreme flares tend to occur in specific patterns that repeat over time. We found two key patterns: a 1.7-year cycle and a 7-year cycle that work together to create the identified high-risk periods including intense geomagnetic storms and Ground Level Enhancement events on Earth. Based on these patterns, we predict that the next high-risk window for superflares will occur around 2026–2027, with the southern hemisphere of the Sun being particularly more active.

Key Points:

- We develop a probabilistic spatiotemporal model forecasting S-class flare occurrences during Solar Cycle 25 and beyond
- Positive cross-Laplacian regions act as magnetic energy sinks, identifying sites of flux reconnection that are favorable for S-flares
- S-flares are modulated by 1.7-year and 7-year oscillations, where constructive interference defines the probability of extreme activity

Correspondence to:
V. M. V. Herrera,
vmv@igeofisica.unam.mx

Citation:
Velasco Herrera, V. M., Velasco Herrera, G., Soon, W., Özgüç, A., Babynets, N., Tlatov, A., et al. (2026). A new method for probabilistic spatiotemporal forecasts of solar soft X-ray "S-class" (>X10) superflares. *Journal of Geophysical Research: Space Physics*, *131*, e2025JA034977. https://doi.org/10.1029/2025JA034977

Received 16 DEC 2025
Accepted 31 JAN 2026

Author Contributions:

Conceptualization: V. M. Velasco Herrera
Data curation: V. M. Velasco Herrera, G. Velasco Herrera, A. Özgüç, N. Babynets, A. Tlatov, S. Baliunas, B. Kotan, G. González González, L. A. Bautista Flores, M. Pazos
Formal analysis: V. M. Velasco Herrera, G. Velasco Herrera, W. Soon, A. Özgüç, A. Tlatov, M. Švanda, S. Qiu, G. González González

Investigation: V. M. Velasco Herrera, W. Soon, A. Özgüç, N. Babynets, A. Tlatov, M. Švanda, S. Qiu
Methodology: V. M. Velasco Herrera, G. Velasco Herrera, W. Soon
Resources: V. M. Velasco Herrera
Software: V. M. Velasco Herrera
Supervision: G. Velasco Herrera, N. Babynets
Validation: V. M. Velasco Herrera
Visualization: G. Velasco Herrera, W. Soon, N. Babynets
Writing – original draft: V. M. Velasco Herrera, W. Soon, N. Babynets
Writing – review & editing: V. M. Velasco Herrera, W. Soon, N. Babynets

1. Introduction

Solar flares arise from nonlinear dynamical processes of magnetic reconnection in the solar atmosphere (e.g., Parker, 1963) and represent among the most energetic manifestations of magnetic energy release in the upper chromosphere and low corona or chromosphere–corona interface (CCI). The Geostationary Operational Environmental Satellites (GOES, Woods et al., 2024) network observes X-ray flares in two spectral bands: Hard X-ray (HXR; 0.05–0.4Å) and Soft X-ray (SXR; 1–8Å). Soft X-ray flares are classified according to their peak flux into categories B (10^{-7} W m^{-2}), C (10^{-6} W m^{-2}), M (1.0^{-5} W m^{-2}), and X (10^{-4} W m^{-2}). Despite their relatively frequent occurrences, accurate prediction of powerful SXR flares (>X10) remains a long-running challenge in heliophysics (Bai & Sturrock, 1989; Bloomfield et al., 2012; Leka et al., 2019). Even for moderate X-class flares (1.0×10^{-4}—10×10^{-4} W m^{-2}; see Table 1 for some of the more prominent events during 2024 and 2025) while they exhibit some regularity, robust methodologies for statistical SXR prediction remain elusive.

Among these abrupt energetic flares, super-flares or S-class flares (>X10) constitute the most energetic category routinely observed (Tan et al., 2025). These extreme events are comparatively rare yet carry significant implications for both fundamental solar physics and operational space weather forecasting. The uniform recalibration of GOES SXR flare data spanning 1975–2022 by Hudson et al. (2024) provides an invaluable database for extreme event studies.

Previous analyses have revealed important patterns in solar flare occurrence. Tan et al. (2025) analyzed GOES soft X-ray records from 1975 to 2024, identifying 37 S-flares and noting their preferential occurrence during the descending phases of solar cycles. They proposed the existence of a persistent low-latitude active zone that spans successive cycles and interacts with newly emerging active regions during the declining phase of the 11-year solar activity cycle, creating favorable magnetic conditions for powerful eruptions. This empirical picture connects large-scale solar dynamo processes with episodic extreme flare activity, offering potential predictive insight for the most energetic solar events.

Complementary statistical analyses reveal additional patterns in flare occurrence. Prasad et al. (2021); Prasad et al. (2022) examined SXR flares from 1976 to 2019 (Cycles 21–24), finding consistent southern hemisphere dominance across all four cycles, with the 10°–20° latitudinal band being most productive. Their time-latitude analysis showed that high-intensity flares rarely occur near the equatorial region (0°–5°), whereas low-intensity flares exhibit higher frequency there. In contrast, East-West distributions showed no persistent longitudinal enhancement. However, a recent analysis by Korsós and Erdélyi (2025) shows that *X*-class flares do preferentially emerge along relatively stable (for up to four to nine Carrington rotations) Active Longitude (AL) regions with concentrated energetic flares and complex magnetic fields—highlighting their critical role in major solar eruptions. Xiong et al. (2021) conducted statistical analysis of SXR flares between 1986 and 2017, revealing significant cycle-to-cycle variations in occurrence rates, temporal distributions, and duration characteristics. Solar Cycle 22 emerged as particularly active with frequent large flares, while Cycles 23 and 24 showed progressively weaker activity. These observed spatial patterns and temporal trends provide valuable, albeit rather minimal and vague, constraints for solar dynamo models and space weather prediction.

The relationship between SXR flares and sunspot group characteristics across Cycles 21–25 was systematically investigated by Lin et al. (2023), who reported significant North-South asymmetry in both flare and sunspot group distributions, with an overall southern hemisphere dominance. Supporting the hemispheric asymmetry findings, V. Velasco Herrera et al. (2025) analyzed a new hemispheric Solar Flare Index (hSFI) from 1937 to 2024, reporting Northern Hemisphere predominance during Cycles 17–21 that switched to Southern Hemisphere dominance in Cycles 22–25.

In a comprehensive operational context, Camporeale and Berger (2025) verified NOAA Space Weather Prediction Center solar flare forecasts over a 26-year period (1998–2024), finding that operational forecasts do not outperform simple baselines (i.e., no-change in the futures or past averages), exhibit poor calibration, and demonstrate critical failures in high-stakes scenarios. These results have significant implications for space weather operations and human spaceflight safety.

Historical events underscore the catastrophic potential of extreme solar activity. The 1859 Carrington event (Hayakawa et al., 2023) and more recent extreme flares like the X45.9 event of 11 July 1978 recently reclassified

Table 1
Summary of Moderate Soft X-Ray Flares and Their Associated Active Region (AR) Observed During Geomagnetic Storms in May and October 2024 as Well as November 2025

Year	Month	Day	X-class	AR	SFI
2024	5	3	X1.6	13,663	18.03
2024	5	5	X1.3	13,663	
2024	5	5	X1.2	13,663	79.83
2024	5	6	X4.5	13,663	184.10
2024	5	8	X1.0	13,663	
2024	5	8	X1.0	13,664	
2024	5	8	X1.0	13,664	
2024	5	8	X1.0	13,664	116.92
2024	5	9	X2.2	13,664	
2024	5	9	X1.1	13,664	42.33
2024	5	10	X3.9	13,664	55.31
2024	5	11	X5.8	13,664	
2024	5	11	X1.5	13,664	38.42
2024	5	12	X1.0	13,664	8.60
2024	5	14	X1.7	13,664	
2024	5	14	X1.2	13,664	
2024	5	14	X8.7	13,664	8.25
2024	5	15	X2.9	13,685	1.27
2024	10	1	X7.1	13,842	19.35
2024	10	3	X9.0	13,842	8.10
2024	10	7	X2.1	13,842	11.71
2024	10	9	X1.4	13,842	
2025	11	9	X1.7	14,274	6.33
2025	11	10	X1.2	14,274	0.92
2025	11	11	X5.1	14,274	3.00
2025	11	14	X4.0	14,274	4.56

Note. Additionally, the daily values of the full-disc Solar Flare Index (SFI) are shown for the same dates on which the moderate soft X-ray flares were reported (see Section 2 for the sources of all the data used in this paper and discussion notes in the Introduction concerning the two >X10 flares detected on the far-side of the Sun on 14 and 20 May 2024 by the Solar Orbiter mission).

by Hudson et al. (2024) demonstrate the Sun's persistent capacity for producing abrupt magnetic flare eruptions with profound technological consequences.

Table 1 additionally reports the daily values of the full disc Solar Flare Index (SFI). The maximum SFI recorded over nearly a century of continuous monitoring reached 184.1 on 6 May 2024 contemporaneous with an X4.5 SXR flare. The SXR events of –X8.7 and X9.0– occurred during the major geomagnetic disturbances of May 2024 and October 2024, respectively. Although none of these flares exceeded the X10 threshold, their occurrence indicates that Solar Cycle 25 retains sufficient free magnetic energy in active-region complexes to sustain episodes of high-intensity (S-class) flare activity throughout its maximum and into the early declining phase. In Section 4.10 and Figure 7a, we analyze two newly identified S-class flares originating on the far side of the Sun, with estimated GOES classes: (a) an X11.1 flare on 14 May 2024, and (b) an X16.5 flare on 20 May 2024. Both events were detected by the Solar Orbiter mission and reported by Stiefel et al. (2025) and Kontogiannis et al. (2025).

Furthermore, these events further emphasized societal vulnerability to space weather, producing intense aurorae at unusually low latitudes and transient impacts on communications and satellite services. The solar physics community should actively investigate whether their occurrence follows deterministic patterns or represents essentially stochastic phenomena. This study develops a comprehensive, probabilistic spatiotemporal forecasting framework to address this fundamental question.

This paper is structured as follows. Section 2 describes the GOES SXR flare data, the S-flare catalog, and supplementary solar activity indices used in this study. Section 3 details our methodology that is built on two pillars: (a) a novel vector calculus framework (Gradient, Laplacian, and Cross-Laplacian diagnostics) applied to butterfly diagrams for spatial analysis, and (b) wavelet spectral analysis combined with a Bayesian Least-Squares Support Vector Machine (LS-SVM) model to identify and project the temporal oscillations modulating extreme activity. Section 4 presents the results, beginning with the spatial patterns derived from the butterfly diagram analysis, followed by the temporal modulation of S-flares and the validation of the oscillation model using historical Ground Level Enhancement (GLE) events. This section culminates in the presentation of our integrated spatiotemporal probabilistic forecast for S-class flares in Solar Cycles 25 and 26 as well as a discussion of limitations of current analyses and of potential future work. Finally, Section 5 discusses the physical implications of our findings, compares our approach to existing forecasting paradigms, and summarizes our conclusions.

2. Data

2.1. Solar Soft X-Ray Flares

For this paper, we have compiled a comprehensive catalog of GOES SXR flares from 1975 to November 2025 using multiple sources to ensure completeness:

- Reuven Ramaty High Energy Solar Spectroscopic Imager, NASA (https://hesperia.gsfc.nasa.gov/goes/).
- National Geophysical Data Center (NGDC) (https://www.ngdc.noaa.gov/stp/space-weather/solar-data/solar-features/solar-flares/x-rays/goes/xrs/).
- World Data Center for Solar-Terrestrial Physics (http://www.wdcb.ru/stp/solar/solar_flare_events.html).
- Archival Solar Flares Catalog (Berretti et al., 2025).

Table 2
List of S-Flare Events (Tan et al., 2025)

S-flare events 1–20							S-flare events 21–37						
E	Y	M	D	L	AR	SFI	E	Y	M	D	L	AR	SFI
1	1978	7	11	20	1,203	58.17	21	1991	6	9	34	6,659	30.44
2	1980	11	6	−12	2,776	91.86	22	1991	6	11	31	6,659	37.54
3	1982	6	3	−9	3,763	27.04	23	1991	6	15	33	6,659	40.21
4	1982	6	6	−9	3,763	25.40	24	1992	11	2	−26	7,321	13.70
5	1982	7	12	11	3,804	85.09	25	1997	11	6	−18	8,100	11.30
6	1982	12	15	−10	4,026	28.67	26	2001	4	2	19	9,393	30.14
7	1982	12	17	−8	4,025	30.57	27	2001	4	15	−20	9,415	13.19
8	1984	4	24	−12	4,474	40.38	28	2003	10	28	−16	10,486	144.32
9	1984	5	20	−9	4,492	17.92	29	2003	10	29	−15	10,486	31.87
10	1989	3	6	35	5,395	43.37	30	2003	11	2	−14	10,486	30.47
11	1989	8	16	−18	5,629	18.35	31	2003	11	4	−19	10,486	12.09
12	1989	9	29	−20	5,698	19.53	32	2005	1	20	14	10,720	23.75
13	1989	10	19	−27	5,747	88.96	33	2005	9	7	−11	10,808	20.60
14	1990	5	24	33	6,063	12.00	34	2006	12	5	−7	10,930	15.25
15	1991	1	25	−16	6,471	32.45	35	2011	8	9	17	11,263	14.79
16	1991	3	4	−20	6,538	6.54	36	2017	9	6	−8	12,673	90.29
17	1991	3	22	−26	6,555	38.06	37	2017	9	10	−8	12,673	
18	1991	6	1	25	6,659	21.50							
19	1991	6	4	30	6,659	16.35							
20	1991	6	6	33	6,659	47.15							

Note. Event (E), year (Y), month (M), day (D), latitude (L), and active region (AR). Additionally, the daily values of the Solar Flare Index (SFI) are shown for the same dates on which the S-class flares were reported.

- Published records of S-flares from Solar Cycles 21–24 (Hudson et al., 2024; Janssens et al., 2025; Tan et al., 2025).

Following the uniform recalibration to pre-GOES-16 data by Hudson et al. (2024), we removed oversaturated *B*-class flare records between 2003 and 2006, which does not affect the forecasting of S-flares or vector calculus analysis described below. The final database contains a grand total of 95,627 events with information on year, month, day, latitude, and SXR class, including the 37 S-flares recently reported by Tan et al. (2025). Additionally, we have converted the S-flares events into a binary digital signal (S) for wavelet analysis and Machine Learning (ML) applications:

$$S_n = \begin{cases} 1, & \text{S-flares event} \\ 0, & \text{noS-flares event} \end{cases} \quad (1)$$

with n = (1, 2, …, 37). The S-flares events are listed in Table 2 and the chronology is shown in the timeline (Figure 1). This uniform set of data records permits us to study the spatiotemporal patterns underlying the solar S-class flare events.

2.1.1. Timeline of Flare Activity/Events

Figure 1 presents the temporal distribution of the 37 S-flare events detected by GOES between 1978 and 2025 (see Table 2). The last S-flare event was recorded 10 September 2017. This visualization reveals clear epochs of enhanced and reduced activity, with the most active years being 1991 (9 events), 2003 (4 events), and 1989

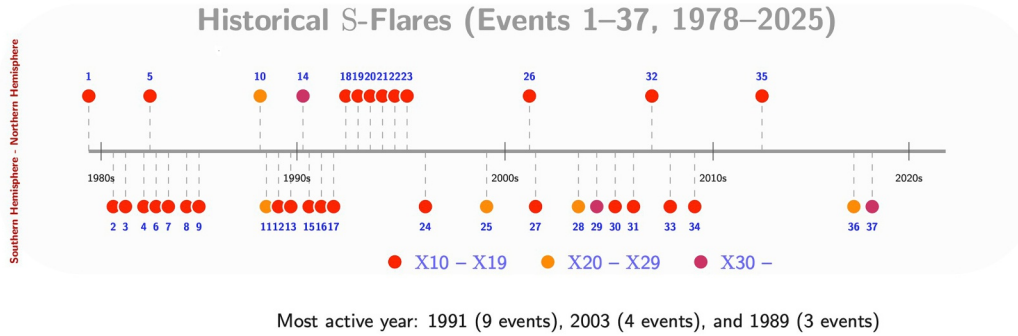

Figure 1. Timeline of solar S-flares. The figure shows the distribution of 37 S-flares from 1978 to 2025, categorized by intensity. The most active years were 1991 with 9 events, 2003 with 4 events, and 1989 with 3 events. S-flares are grouped into three classes: X10–X19 (moderate extreme), X20–X29 (severe extreme), and X30– (ultra extreme). The last S-flare event was recorded 10 September 2017. Data are compiled from Geostationary Operational Environmental Satellites satellite observations. Northern Hemisphere flares are displayed above the centerline while the Southern Hemisphere flares displayed below.

(3 events). The apparent clustering of these events suggests a recurrence timescale shorter than the 11-year solar cycle, a hypothesis we test quantitatively in Section 4 using wavelet analysis.

The concurrent Solar Flare Index (SFI) values for these S-flare epochs, provided in Table 2, offer a complementary perspective on chromospheric energy release. Notably, the most intense SXR flares coincide with very high SFI values (e.g., SFI = 144.32 for the X25.7 flare on 2003 October 28). However, this intense SXR flare-SFI correspondence is clearly not one to one. The highest SFI on record (184.10 on 6 May 2024, see V. Velasco Herrera et al., 2025, for more details) was not associated with an S-class SXR flare. This disparity underscores that while both indices trace powerful energy release, they sample different atmospheric layers (SFI predominantly the chromosphere, SXR the upper chromosphere and low corona) and thus provide distinct, complementary diagnostics of extreme solar activity. A complete forecasting paradigm must therefore account for the photospheric/chromospheric conditions conducive to energy accumulation (sunspot area and SFI) and the coronal conditions for its explosive release (SXR flares).

This preliminary overview motivates our two-pronged methodology. First, to identify the spatiotemporal zones of magnetic energy accumulation using butterfly diagram diagnostics (Sections 3.1 and 4.1–4.7). Second, to identify the temporal windows of heightened probability by analyzing the underlying oscillations in flare occurrence (Sections 4.8 and 4.9).

2.2. Supplementary Solar Activity Indices

Additionally, we use the following solar indices:

1. hSFI (https://doi.org/10.7910/DVN/TSQEPB, https://doi.org/10.7910/DVN/C1L8ZX).
2. The dates of the GLEs events (https://www.ngdc.noaa.gov/stp/space-weather/interplanetary-data/cosmic-rays/ground-level-enhancements/ground-level-enhancements.txt, https://www.nmdb.eu/nest/).
3. The daily sunspot area (Royal Greenwich Observatory and USAF/NOAA) (http://solarcyclescience.com/activeregions.html).

3. Method

3.1. Vector Analysis of Solar Butterfly Diagrams

We developed a novel cross-vector analysis to quantify spatiotemporal correlation patterns from different solar activity data sets. Our approach enables quantitative comparison of scalar or vector fields using the Hadamard products to calculate cross-gradient and divergence fields.

- *Data Processing and Field Construction*: Solar flare and sunspot area data are scalar fields (ϕ), and were mapped onto a unified time-latitude grid. Discrete events were converted into continuous density fields

through 2D histogramming followed by Gaussian kernel smoothing, preserving large-scale spatiotemporal structures while reducing high-frequency noise (Bathe, 1996; Zienkiewicz et al., 2005).

- *Grid Resolution*:
  - Temporal bins: 160 bins spanning 1975–2025
  - Latitudinal bins: 120 bins covering the full solar latitude range (−90° to 90°)
- *Gaussian Smoothing*:
  - Kernel size: 7×7 pixels
  - Standard deviation: $\sigma = 2.0$
- *Field Computation*: For each data set, we computed:
  - Gradient fields $\left(\mathcal{G}_i = \nabla\phi_i\right)$, capturing the direction and rate of maximum density change in time-latitude space.
  - Laplacian fields $\left(\mathcal{L}_i = \nabla^2\phi_i\right)$, identifying local source (positive) and sink (negative) regions.
  - Derivatives were evaluated using finite difference schemes on the structured grid (Hughes, 2000; Zienkiewicz et al., 2005).
- *Cross-Field Analysis*: The core innovation involves computing the Hadamard products (see Soon et al., 2018, for more details on Hadamard algebra) between corresponding fields.
- *Cross-Gradient*: $\mathcal{G}_{1,2} = \nabla\phi_1 * \nabla\phi_2$

Measures pointwise alignment in emergence/migration patterns between different magnetic indicators.

- *Cross-Laplacian*: $\mathcal{L}_{1,2} = \nabla^2\phi_1 * \nabla^2\phi_2$

Identifies coupled source-sink dynamics between photospheric and coronal magnetic systems (see Figure 2).

This newly proposed methodology, as summarized in Figure 2, represents a paradigm shift from statistical correlation to physics-informed co-variation analysis, enabling precise identification of regions susceptible to extreme solar flare activity while maintaining interpretability through direct physical diagnostics.

4. Results and Interpretations

4.1. Butterfly Diagram of Solar Soft X-Ray Flares

The classical Maunder butterfly diagram for sunspots (see Figure 3a), has long provided fundamental insights into the latitudinal distribution of sunspot activity across the solar cycle (Maunder, 1904). The photospheric butterfly diagram shows that sunspots emerge at mid-latitudes and migrate toward the equator over the 11-year solar cycle (i.e., the Spörer's Law, Carrington, 1858). Solar cycle intensity determines the diagram's structure. Stronger cycles start at higher latitudes and display wings with greater latitudinal width. Furthermore, consecutive cycles overlap by 1–2 years; greater overlap forecasts a more intense subsequent solar cycle, while weak cycles show minimal transitional overlaps and narrower wings (Norton et al., 2023). We classify the sunspot areas into seven categories, with those having areas >1200 μHem highlighted as black dots in Figure 3a. These large sunspot areas are of great interest due to their relationship with the active regions (AR) that are the origin of S-flares.

We extend the classical Maunder butterfly framework to solar flare activity in the upper chromosphere and low corona or the chromosphere–corona interface (CCI), by constructing a diagram that tracks the spatiotemporal evolution of SXR flares over nearly five decades (Figure 3b). The butterfly diagram of solar SXR flares reveals the characteristic of equatorward migration of flare activity, mirroring the photospheric pattern but with distinct "energy-release" signatures.

Each solar cycle initiates flare activity around mid-latitudes (~±40°) and progressively migrates toward the equatorial region (~±5°) as the cycle evolves, following Spörer's Law (Carrington, 1858). This systematic progression reflects the underlying dynamics of magnetic flux emergence and transport. The overlap between consecutive cycles provides evidence for the underlying operation of the magnetohydrodynamic solar dynamo (Parker, 1955). This diagram exhibits remarkable symmetry and regularity across Cycles 21–24, with dense, well-defined activity bands. Cycle 25 displays developing amplitude and spatial extent around ±40°, confirming the cycle's progression and aligning with dynamo-based predictions.

The butterfly diagram provides a window into solar dynamo dynamics. The latitudinal migration pattern reflects the transport of toroidal magnetic flux from generation zones at mid-latitudes toward the equator via meridional circulation (Hathaway & Upton, 2014). The activity bands trace the emergence of this subsurface magnetic field

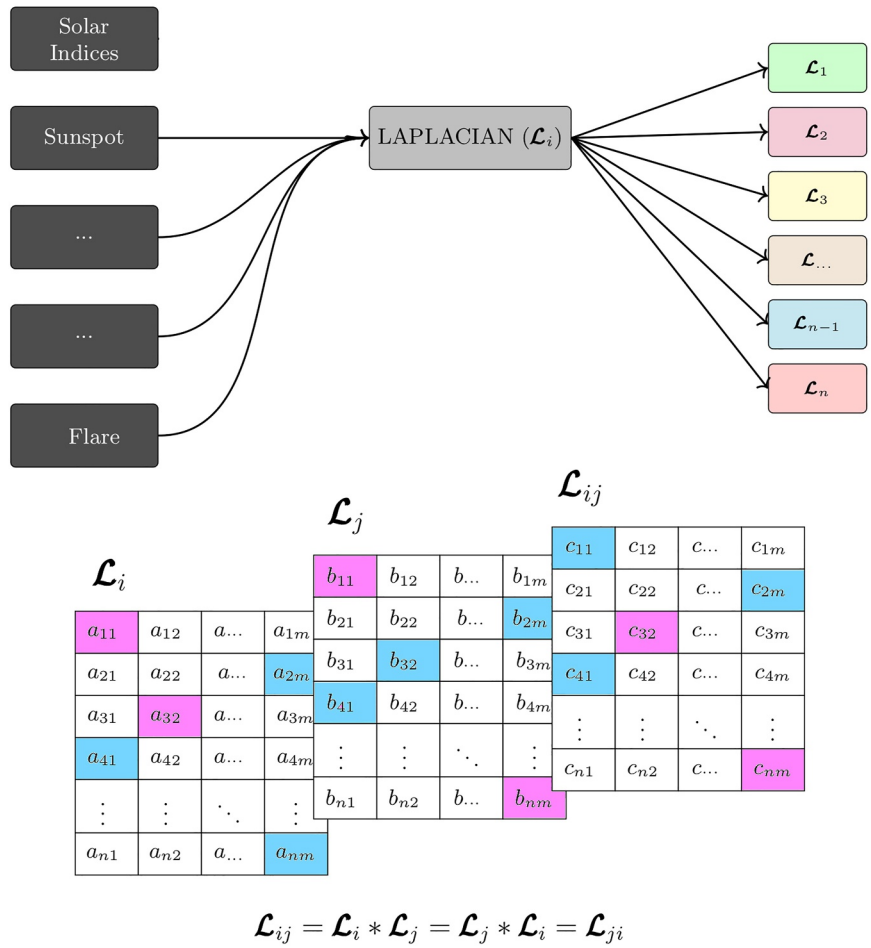

Figure 2. Conceptual diagram of the Laplacian and Cross-Laplacian analysis applied to solar butterfly diagrams. The Laplacian operator ($\mathcal{L}$) applied to a scalar field (e.g., sunspot area density) measures the local curvature, identifying sources (positive Laplacian, red) where the quantity is locally concentrated and sinks (negative Laplacian, blue) where it is depleted or converging. For the sunspot and flare density fields, a negative Laplacian region can be interpreted as a zone of magnetic flux and energy accumulation–a potential reservoir for extreme activity. The Cross-Laplacian is computed as the Hadamard product ($*$) of the individual Laplacian fields. Its sign reveals the coupling between the photosphere (sunspots) and corona (flares): a positive Cross-Laplacian (red) indicates a co-located energy sink in both layers (i.e., coupled storage), while a negative value (blue) indicates a mismatch. This novel diagnostic physically identifies spatiotemporal domains where the photospheric magnetic configuration is primed to energize the corona, thereby highlighting zones of heightened probability for S-class flares.

through the photosphere, where it forms complex active regions capable of producing energetic flares (Toriumi & Wang, 2019).

Current observations show SXR flares concentrated at mid-high latitudes in the developing Cycle 25. We anticipate increased S-flare occurrence as the cycle approaches maximum around 2026–2027 and overall solar activity migrates equatorward. The appearance of S-flares in this cycle is particularly significant: their occurrence during the ascending phase indicates that Cycle 25's magnetic field possesses sufficient strength and complex magnetic topology to generate extreme flare events.

The synchronized migration of both sunspot area and SXR flare activity confirms that both physical quantities originate from the same source, the emerging toroidal magnetic field. In particularly, the S-flares are strongly co-located with large, complex sunspots and spot groups, which provide the necessary environment for magnetic reconnections. Large area sunspot appearance is more continuous and spread out, while S-flare occurrence is clustered, reflecting their dependence on rapid, complex magnetic configurations rather than just the presence of large or strong magnetic flux emergence. S-flares can show greater latitudinal scatter and may be slightly offset from main active regions, suggesting the most flare-productive active regions develop as the activity bands

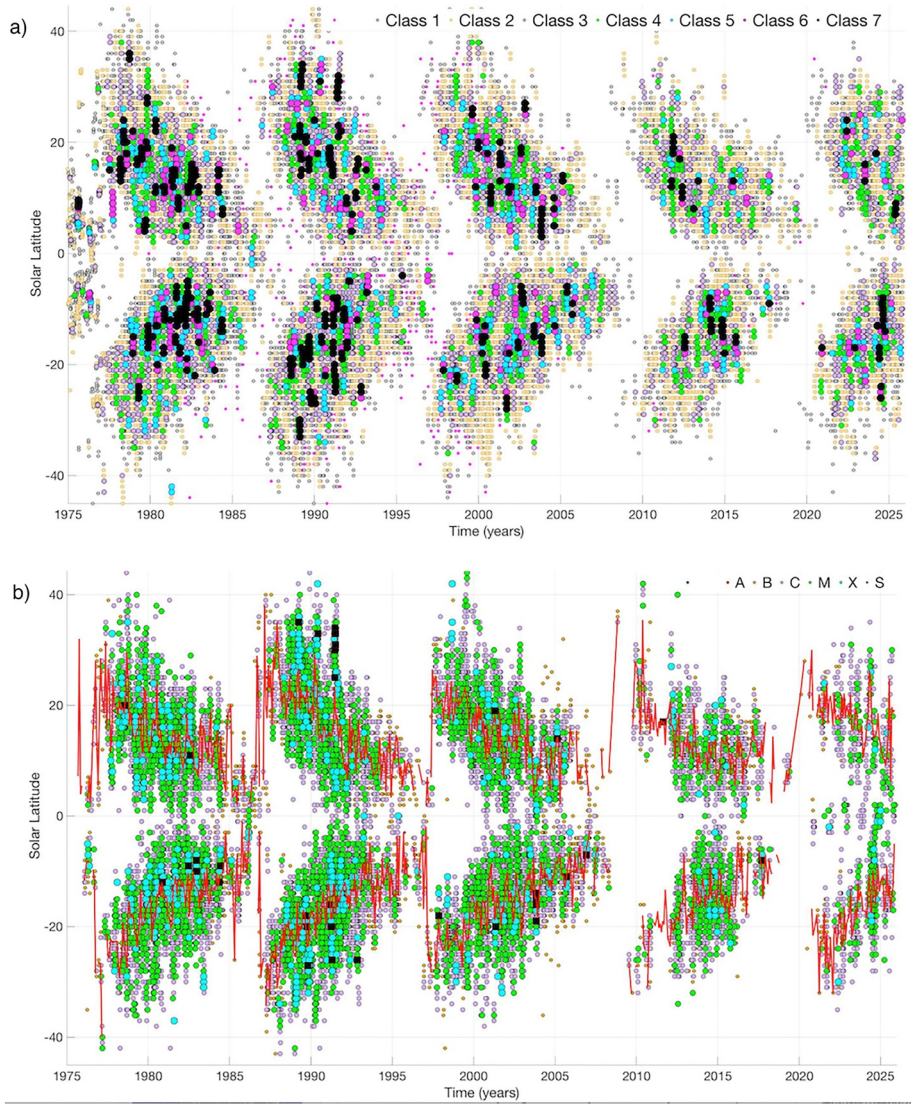

Figure 3. Butterfly diagram of photosphere and upper chromosphere and low corona between 1975 and 2025. (a) Sunspot areas have been classified into 7 classes: class 1 < 50, class 2 50–100, class 3,100–200, class 4 200–400, class 5 400–600, class 6 800–1200 and class 7 > 1200 μHem is highlighted and marked by black dots. (b) Soft X-ray flare activity showing heliographic latitude of solar flare events/activities versus time. Flare classes are color-coded: B (light cyan), C (green), M (blue), X (cyan), and S-flares (black). Red lines trace monthly averaged latitudinal migration in the northern and southern hemispheres, respectively. The systematic equatorward progression reflects solar cycle evolution, with variations in flare occurrence and intensity across decades.

migrate equatorward. The S-class flare activity shows more pronounced north-south asymmetries than sunspots area.

In the following sections, we apply gradient and Laplacian analyses to quantify the correlation between large sunspot areas and S-flares.

4.2. Gradient of the Butterfly Diagram of Soft X-Ray Flares and Sunspot Areas

The butterfly diagram of the upper chromosphere and low corona provides valuable insight into the spatiotemporal evolution of solar magnetic activity, complementing traditional photospheric indicators. While the photospheric butterfly pattern has been investigated since the pioneering work of Maunder (1904), its CCI counterpart reveals distinct signatures of magnetic energy release in the upper solar atmosphere (Vernazza et al., 1981). The gradient of this diagram enhances contrasts in magnetic flux transport and emergence, offering a

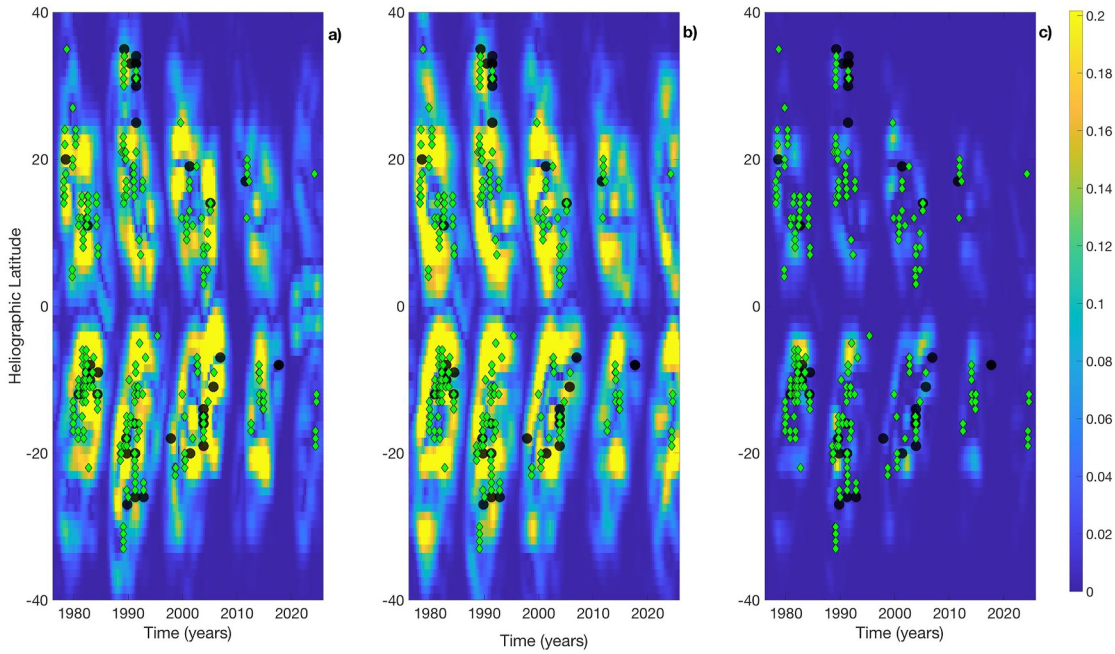

Figure 4. (a) Gradient magnitude of the chromospheric butterfly diagram of soft X-ray flare activity (1975–2025). (b) Gradient magnitude of the photospheric sunspot-area butterfly diagram. S-class flares are shown as black points. (c) Cross-gradient between the flare and sunspot-area gradient fields. Sunspot area >1,200 μHem is highlighted and marked by green dots and S-class flare is shown with black points.

diagnostic closely linked to solar flare productivity (Cliver et al., 2022). The gradient is computed strictly from the latitudinal and temporal distributions of SXR flares and sunspot areas, without incorporating classification or magnitude information from either data set.

4.2.1. Gradient of the Spatiotemporal Distributions of Soft X-Ray Flares

Considering the latitudinal distribution of SXR flares or sunspot areas as a scalar field $\phi_i(\lambda, t)$, its gradient magnitude $\mathcal{G}_i(\lambda, t)$ is a proxy for the migration velocity of solar flare or sunspot distributions in the time–latitude domain. Here $i = 1, 2$ corresponds to SXR flares and sunspot areas, respectively.

Regions of large gradient magnitude (yellow in Figure 4) correspond to phases of strong migratory dynamics, where solar flares distributions shift significantly in latitude. In contrast, regions with small gradient magnitude (blue zones in Figure 4) indicate intervals of spatial confinement or slow temporal evolution. In this sense a large gradient is an indicator for a rapid migration and strong spatiotemporal variation, while a small gradient is representing a stable or weakly evolving distributions. The gradient magnitude of the SXR flare butterfly diagram ($\mathcal{G}_1$) is shown in Figure 4a.

We analyze the temporal evolution of $\mathcal{G}_1(\lambda, t)$ from 1975 to 2025 (Solar Cycles 21–25), focusing on its relationship with S-class flares and large sunspot regions. Figure 4 reveals three principal characteristics:

1. *Solar-cycle modulation.* The gradient field exhibits clear 11-year periodicity, with activity bands migrating from mid-latitudes (±40°) toward the equator (±10°), consistent with established magnetic-flux transport patterns. Each cycle shows ramp-like gradient intensification during its rising phase, indicating strengthening magnetic field gradients (Leamon et al., 2022).
2. *Spatiotemporal organization of S-class flares. S*-class flares cluster at mid-latitudes (±30°–40°) during cycle initiation, coinciding with new magnetic flux emergence (Nandy, 2006). During termination phases, they concentrate near the equator (within ±10°) where magnetic flux cancels and reorganizes. The gradient field traces organized equatorward flux migration via meridional circulation (Hathaway & Upton, 2014), latitudinal shear from differential rotation (Beck, 2000), and toroidal flux emergence consistent with solar dynamo predictions (Charbonneau, 2020).

3. *Physical significance of gradient structures.* *S*-flares preferentially occur in strong-gradient regions, identifying sites of steep magnetic-field gradients and current sheets (Pontin & Priest, 2022), environments favorable for reconnection-driven energy release, zones of elevated magnetic complexity conducive to major flaring (Leka et al., 2019), and locations with substantial non-potential magnetic energy reservoirs (Jing et al., 2010).

4.2.2. Cycle-By-Cycle Analysis

The systematic CCI gradient evolution provides valuable constraints for solar dynamo and flux transport models (Charbonneau, 2020). The persistent correlation between gradient structures and S-flare occurrence highlights magnetic gradients as a key parameter for forecasting solar flares (Bobra & Couvidat, 2014).

S-flare concentration in specific latitudinal bands during different cycle phases suggests both emergence-dominated (mid-latitude) and cancellation-dominated (equatorial) processes contribute to intense flare production (Toriumi & Wang, 2019). This dual-mode scenario has important implications for understanding flare triggers and their relationship to global magnetic field evolution.

Cycle-specific characteristics reveal distinct magnetic configurations:

- *Solar Cycle 21* (9 S-flares: 2N, 7S): Well-defined gradient structure with continuous equatorward migration, suggesting symmetric hemispheric activity and organized flux emergence.
- *Solar Cycle 22* (16 S-flares: 8N, 8S): Similar to Solar Cycle 21 but with higher S-flare density at mid-latitudes, indicating enhanced magnetic complexity.
- *Solar Cycle 23* (10 S-flares: 3N, 7S): Complex gradient structure with multiple bands and dispersed S-flare distribution, implying distributed magnetic activity and possible multipolar configurations.
- *Solar Cycle 24* (2 S-flares: 1N, 1S): Weak gradient intensity and reduced S-flare density, reflecting lower magnetic energy and simplified topology.
- *Solar Cycle 25*: Developing gradient patterns with enhanced southern hemisphere activity, suggesting increasing magnetic complexity approaching maximum.

4.2.3. Spatial Localization of Flares Across Solar Cycles

Our analysis reveals that S-class flares exhibit strong spatial correlation with gradient extrema in the butterfly diagram (see Figure 4a). These S-flares consistently occur at locations corresponding to maximum or minimum values of the spatiotemporal gradient, representing regions of peak and minimal migration velocities in both hemispheres across all solar cycles. This empirical relationship provides the first observational constraint for identifying probable spatial domains of S-flare occurrence in Solar Cycle 25. Gradient extremum locations serve as primary indicators of flare-prone regions. While the gradient field identifies zones of rapid morphological change, the Laplacian operator ($\mathcal{L}$) applied to the butterfly diagram offers complementary physical insight into magnetic energy distribution.

The combined spatiotemporal approach enables comprehensive prediction of both timing and latitudinal distribution for S-flares in Cycle 25, advancing beyond purely spatial or temporal methods. Having established SXR flare migration patterns through gradient analysis, we now examine the underlying magnetic field responsible for their generation by calculating the gradient of the sunspot area butterfly diagram, which serves as a proxy for toroidal field evolution in the solar dynamo.

4.3. Gradient of the Sunspot-Area Butterfly Diagram

The sunspot-area butterfly diagram serves as a proxy for the spatiotemporal evolution of the toroidal magnetic field component generated by the solar dynamo (Feynman, 1982; Parker, 1955). Its gradient magnitude $\mathcal{G}_{\mathrm{I}}(\lambda, t)$ quantifies the rate of change of flux emergence in both latitude and time. Regions with large $\mathcal{G}_{\mathrm{I}}$ values (yellow areas in Figure 4b) identify zones where magnetic flux emergence evolves rapidly, highlighting the equatorward migration of activity belts, rapid amplification or decay of toroidal flux, and boundaries of newly emerging active complexes. The gradient thus provides a diagnostic of the local dynamical state of the toroidal field as manifested at the solar surface. High $\mathcal{G}_{\mathrm{I}}$ values may indicate active regions where magnetic shearing occurs through processes such as magnetic reconnection and flux emergence.

Complementarily, the SXR flare distribution (Figure 3b) reflects the spatiotemporal reconfiguration of the upper chromosphere and low corona magnetic fields and the conversion of magnetic free energy into radiation. Strong $\mathcal{G}_1$ values identify regions where solar flare productivity changes rapidly, signaling energization or relaxation of the upper chromosphere and low corona fields, evolution of active-region complexes, and intervals of enhanced magnetic shearing or helicity injection. The gradient magnitude thus traces the dynamical evolution of the upper chromosphere and low corona magnetic system driven by interactions between newly emerged and pre-existing magnetic fields.

4.4. A New Gradient-Coupling Diagnostic: The Cross-Gradient

We introduce the *cross-gradient* as a novel diagnostic quantifying local co-variance between flux emergence (sunspot area) and energy release in the upper chromosphere and low corona (SXR flare). Defined as the Hadamard product ($*$) of their respective gradients (see, e.g. Soon et al., 2018, for more details on the Hadamard algebra):

$$\mathcal{G}_{1,2}(\lambda,t) = \mathcal{G}_1(\lambda,t) * \mathcal{G}_2(\lambda,t),$$

this quantity becomes large only when both fields exhibit strong, simultaneous spatiotemporal variability. Unlike vector alignment measures, the cross-gradient captures coincident intensity variations.

Physically, high $\mathcal{G}_{1,2}(\lambda,t)$ values (yellow area in Figure 4c) pinpoint regions where toroidal-field emergence and chromospheric-coronal energy-release rates change rapidly in tandem, marking efficient coupling between the solar dynamo and CCI magnetic system. These locations correspond to epochs of intense flux emergence, mixed-polarity interactions, or strong helicity injection that modulate flare productivity. Conversely, low $\mathcal{G}_{1,2}(\lambda,t)$ values (blue area in Figure 4c) indicate either flux emergence without significant coronal energization, or flaring activity unrelated to new emergent flux. The result of the cross gradient between the gradients of the sunspot area and SXR flares is shown in Figure 4c.

The high or low $\mathcal{G}_{1,2}(\lambda,t)$ values may be possible in three scenarios:

- *High* $\mathcal{G}_{1,2}$: Near-simultaneous rapid flux emergence and sharp increase in flare productivity, typically resulting from: (a) emergence of highly twisted flux ropes that immediately destabilize the upper chromosphere and low corona, (b) rapid injection of opposite-polarity flux into pre-existing active regions triggering prompt reconnection, or (c) interaction between newly emergent toroidal flux and previous-cycle field remnants. These scenarios favor extreme flares and coronal mass ejections (CMEs).
- *Low* $\mathcal{G}_{1,2}$ *with high* $\mathcal{G}_2$: Flux emergence without immediate chromospheric-coronal energy release, occurring for simple bipoles with low magnetic shear, rapid dispersal by surface flows, or emergence into magnetically quiet environments. The emerged flux may contribute to flare only after subsequent surface evolution.
- *Low* $\mathcal{G}_{1,2}$ *with high* $\mathcal{G}_1$: Chromospheric-coronal activity driven by reconfiguration of pre-existing non-potential fields without new flux emergence (e.g., flux cancellation or tether-cutting in mature active regions). Here, photospheric area remains stable while coronal diagnostics show strong variability.

The cross-gradient $\mathcal{G}_{1,2}$ provides a novel tool for probing dynamical connectivity between dynamo-driven toroidal-field evolution and chromospheric-coronal energy release. Combined with gradient diagnostics, it establishes a physically motivated framework linking subsurface magnetic field generation to atmospheric manifestations. When integrated with vector magnetograms and event-level tracking, this approach offers a promising pathway to quantify solar dynamo coupling between surface and chromospheric-coronal activity.

Figure 4 presents the gradient analyses/results of the butterfly diagrams, providing a diagnostic of the spatiotemporal dynamics associated with S-class flares. Panel (a) shows the gradient magnitude of the SXR flare density field. Regions of high gradient (yellow) correspond to epochs and latitudes where the flare distribution undergoes rapid migration or intensification. The S-flares (black dots) are conspicuously clustered within these high-gradient zones, indicating that extreme flares preferentially occur during intervals of sharp dynamical evolution in the global flare pattern.

Panel (b) displays the analogous gradient magnitude for the sunspot area density field. This traces the rapid emergence and transport of photospheric magnetic flux. The largest sunspot groups (area >1200 μHem, green

dots) also tend to reside in regions of pronounced gradient, aligning with the expected behavior of active region complexes that are sources of major activity.

The core of our dynamical coupling diagnostic is shown in Panel (c): the cross-gradient, computed as the pointwise product of the individual gradient fields. This quantity is large only where both the flare and sunspot distributions exhibit strong, simultaneous local variations. The striking result is that S-flares occur almost exclusively within the high positive values (yellow regions) of the cross-gradient field. This reveals that extreme flare activity is tightly linked to epochs and latitudes where the photospheric flux emergence (sunspots) and the coronal energy release (flares) are undergoing rapid, co-located changes. Physically, these zones likely represent sites of intense magnetic shear, rapid flux emergence into pre-existing fields, or strong sunspot rotation, all configurations conducive to building and abruptly releasing non-potential magnetic energy.

The gradient analysis shown in Figure 4 establishes that S-class flares are not randomly distributed but are strongly localized in regions of high spatiotemporal dynamics in both the photospheric and coronal activity patterns. The cross-gradient specifically identifies coupled dynamical evolution between these layers as a key environmental precursor for extreme flares.

4.5. Laplacian Analysis of Soft X-Ray Flare Butterfly Diagram

Building on the characterization of the chromospheric-coronal gradient field and its temporal evolution across solar cycles, we now examine the Laplacian ($\mathcal{L}$) of the SXR flares.

The Laplacian operator applied to the SXR flare ($\mathcal{L}_1$) butterfly diagram quantifies the local curvature of the scalar field associated with flare migration patterns. This mathematical construct reveals fundamental aspects of the acceleration dynamics in flare latitudinal migration and serves as a physical diagnostic for regions of magnetic energy concentration and dissipation.

Indeed we find that $\mathcal{L}_1$ provides critical insight into the underlying magnetic energy distribution. Negative Laplacian regions, identify local maxima in the flare distribution, plausibly corresponding to zones of magnetic energy accumulation. These regions likely result from magnetic reconnection processes that concentrate magnetic energy in a relatively small spatial volume, creating reservoirs for subsequent energy release. Positive Laplacian regions, correspond to local minima where magnetic field dispersal occurs. In these domains, the magnetic energy undergoes gradual dissipation through the emission of B- to M-class, and soft X-ray flares, representing moderated energy release mechanisms. Zero Laplacian regions, indicate spatially uniform conditions characterized by the absence of net acceleration in the flare migration pattern. These regions represent equilibrium states in the latitudinal distribution of flare activity.

This framework provides a quantitative basis for understanding the spatial organization of magnetic energy build-up and release throughout the solar cycle, with direct implications for solar flare forecasting and ultimately the prediction of space weather conditions. Figure 5a displays the Laplacian of the SXR flare butterfly diagram, revealing distinct positive (red) and negative (blue) regions during each solar cycle. These features correspond to fundamental sources and sinks in the solar magnetic energy budget, respectively.

The positive Laplacian regions (red areas) represent latitudinal domains where magnetic energy is systematically released through SXR flares of B through M classes. These events represent the lower-energy component of the flare energy spectrum and indicate ongoing, moderate magnetic dissipation processes. Conversely, the negative Laplacian regions (blue areas) identify zones of magnetic reconnection and non-potential magnetic field configurations. These zones can be plausibly associated with so-called super active regions which are regions with strong and intense magnetic activity and complex magnetic topology (i.e., Bai, 1987; Tian et al., 2002; Dhakal & Zhang, 2023, see also Table 2). These regions serve as reservoirs for accumulating sufficient magnetic energy to power the most explosive solar events, particularly X-class and S-class flares.

As evidenced by the black points/dots in Figure 5a, S-flares exhibit a distinct spatial preference, originating predominantly in proximity to these negative Laplacian regions across all solar cycles and in both hemispheres. This non-random distribution underscores the fundamental physical processes governing flare development. In magnetic reconnection zones and non-potential field regions, the accumulated solar magnetic energy must eventually dissipate. This dissipation manifests as severe flare events, with S-class flares representing a specific manifestation for chromospheric magnetic energy release.

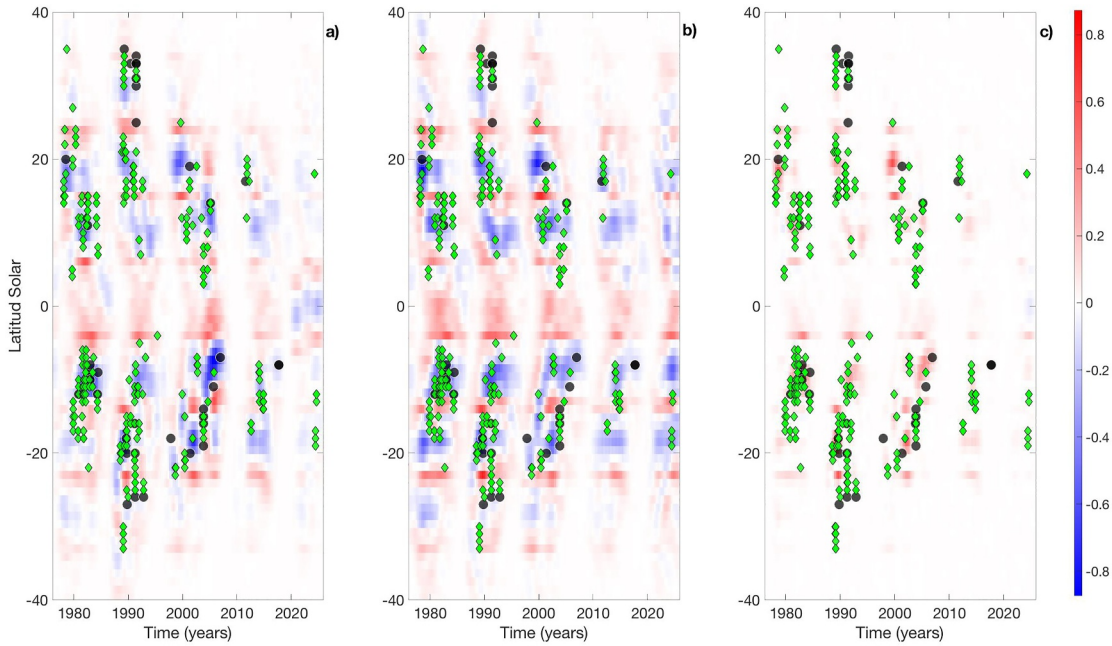

Figure 5. Laplacian of the solar chromospheric-coronal and photospheric butterfly diagram between 1975 and 2025. (a) Soft X-ray flares. (b) Sunspot area. (c) Cross-Laplacian. Large sunspot area >1200 μHem is show in green dots and S-flares in black dots.

Regions exhibiting negative Laplacian characteristics but lacking S-flare activity typically develop lower X-class flares. While not the focus of this investigation, these events represent alternative energy release pathways. Our analysis concentrates specifically on the spatial and temporal forecasting of S-flares. In the ongoing Solar Cycle 25, we observe the development of negative Laplacian regions (blue areas) indicative of significant magnetic energy accumulation through reconnection processes. Based on our spatial analysis, we predict high probability of S-flare occurrence within these regions, particularly those developing between 2026 and 2027.

Continuous monitoring of SXR flare migration patterns remains essential due to the potential space weather impacts associated with accumulated magnetic energy release. The subsequent geomagnetic storms can significantly affect human technological systems, underscoring the practical importance of these forecasts.

4.6. Laplacian Analysis of Sunspot Area Butterfly Diagram

After analyzing the Laplacian of the SXR flare, we will now describe the Laplacian results for the sunspot area $(\mathcal{L}_2)$ shown in Figure 5b and the interpretation is as follows:

1. *Cycle-synchronized migrating sources.* The Laplacian $(\mathcal{L}_2)$ shows bands of positive curvature emerging at mid-latitudes $(\sim\pm30°-40°)$ and migrating equatorward over the cycle. These bands identify the primary sites of flux emergence and agree with the expected behavior of toroidal flux emergence and flux transport by meridional circulation.
2. *Hemispheric asymmetries and phase shifts.* By comparing the northern and southern hemisphere Laplacian different flux dispersal in the two hemispheres.
3. *Localization of large active regions.* Strong, localized positive Laplacian peaks correspond to epochs and latitudes where large sunspot groups form. Tracking the latitude of Laplacian maxima per cycle yields statistics of emergence latitude and its evolution.
4. *Sink regions and flux cancellation.* Extended areas of negative Laplacian identify latitudinal zones and time epochs of flux dispersal/cancellation; these often follow the passage of large active regions and may precede reduced flare productivity locally.

4.7. Cross-Laplacian Between Soft X-Ray and Sunspot Area

To analyze the coupling between photospheric magnetic-flux emergence and chromospheric-coronal energy release, we analyze the cross-Laplacian ($\mathcal{L}_{12}$) constructed from the scalar fields of SXR emission (ϕ_1) and sunspot area (ϕ_2). While the individual Laplacians describe the local curvature of each field, the cross-Laplacian isolates the non-linear spatiotemporal coherence (or co-variance) between them. This operator therefore serves as a diagnostic of the photosphere and upper chromosphere and low corona respond to each other across Solar Cycles 21–25.

We defined the Cross-Laplacian, as the Hadamard product of the individual Laplacians from the sunspot and SXR flare butterfly diagrams:

$$\mathcal{L}_{1,2}(\lambda,t) = \mathcal{L}_1(\lambda,t) * \mathcal{L}_2(\lambda,t) \tag{2}$$

provides a fundamental measure of spatiotemporal coupling between the photosphere and corona. Its physical interpretation requires understanding the implications of the algebraic sign of the product described as follows.

4.8. Positive Cross-Laplacian Regions ($\mathcal{L}^+$, Red in Figure 5c)

A positive Cross-Laplacian indicates curvature coherence between both fields, manifesting in two physically distinct scenarios:

1. $\mathcal{L}_1 > 0$ and $\mathcal{L}_2 > 0$: Both fields exhibit positive Laplacian, corresponding to regions of magnetic energy dispersal or dissipation.
2. $\mathcal{L}_1 < 0$ and $\mathcal{L}_2 < 0$: Both fields display negative Laplacian, identifying co-located sinks of magnetic flux and flare energy.

This second scenario is physically relevant for S-flares. These regions represent zones of simultaneous magnetic energy accumulation in the photosphere (manifested as large sunspot groups) and in the corona (setting the stage for extreme flares). The presence of large active regions (>1200 μHem) in these zones corroborates their role as reservoirs of non-potential energy.

4.9. Negative Cross-Laplacian Regions ($\mathcal{L}^-$, Blue in Figure 5c)

A negative Cross-Laplacian occurs when $\mathcal{L}_1$ and $\mathcal{L}_2$ have opposite signs, revealing anti-correlated curvature evolution that indicates decoupling between photospheric and coronal processes. Possible physical scenarios include:

- Emergence of weak/fragmented magnetic flux with minimal coronal impact
- Coronal restructuring lacking clear photospheric signatures
- Photospheric shearing without substantial sunspot area changes
- Open magnetic topologies that inhibit energy confinement

The consistent association of S-flares with red Cross-Laplacian regions ($\mathcal{L}^+$) where both individual Laplacians are negative provides a robust diagnostic for identifying spatiotemporal domains of high probability for extreme flares. This condition represents a vertically coupled magnetic configuration where energy accumulated in the photosphere can be efficiently transferred and released in the corona through reconnection processes.

Furthermore, the consistent latitudinal co-location of S-class flares with negative cross-Laplacian regions and large sunspot areas suggests that $\mathcal{L}^+$ identifies latitudes and times with enhanced S-flare probability (Figure 5c). These zones exhibit magnetic complexity conducive to non-potential energy accumulation and reconnection.

We interpret the positive cross Laplacian ($\mathcal{L}^+$) as a physical sink where magnetic flux converges or reconnection occurs. This is supported by the presence of both S-class flares and numerous smaller SXR flares within these domains. Smaller flares represent moderate energy release, while S-class events manifest catastrophic release of accumulated magnetic energy.

Table 3
Physical Interpretation of the Gradient, Laplacian, and Cross-Laplacian Signs

Operator	Mathematical meaning	Physical interpretation in solar context	Implication for S-flare forecasting
Gradient Magnitude			
High	Steep local spatial/ temporal change	Zone of rapid migration, emergence, or intensification of activity.	Identifies dynamically active regions where magnetic shear and stress are likely building.
Low	Gentle or uniform variation	Quiescent phase or stable activity band.	Lower immediate probability of extreme restructuring.
Laplacian			
$\mathcal{L} > 0$ (Positive)	Local minimum (concave down)	Source or dispersal zone. Magnetic flux or flare activity is locally depleted or spreading out.	Not a primary zone for energy accumulation. Associated with weaker, dissipative activity.
$\mathcal{L} < 0$ (Negative)	Local maximum (concave up)	Sink or accumulation zone. Magnetic flux/energy is locally concentrated.	Key diagnostic. Identifies a potential reservoir for magnetic energy. S-flares show a strong historical preference for these zones.
Cross-Laplacian			
$\mathcal{L}_{12} > 0$ (Positive)	$\mathcal{L}_1$ and $\mathcal{L}_2$ have the same sign.	Coupled photosphere-corona state. Two physically significant scenarios: 1) $\mathcal{L}_1 > 0$, $\mathcal{L}_2 > 0$: Co-located dispersal. 2) $\mathcal{L}_1 < 0$, $\mathcal{L}_2 < 0$: Co-located accumulation sinks.	Highest forecast significance. The case $\mathcal{L}_1 < 0$, $\mathcal{L}_2 < 0$ indicates coupled energy storage in both layers—the optimal configuration for a major eruption. This is our primary spatial filter.
$\mathcal{L}_{12} < 0$ (Negative)	$\mathcal{L}_1$ and $\mathcal{L}_2$ have opposite signs.	Decoupled or transitional state. for example, Photospheric accumulation without coronal response $(\mathcal{L}_2 > 0)$, or coronal activity without clear photospheric driver $(\mathcal{L}_1 > 0)$.	Lower probability for an extreme, coupled eruption. May indicate inefficient energy transfer or uncorrelated processes.

The temporal lead-lag structure of $\boldsymbol{\mathcal{L}}_{12}$ provides insight into causal relationships. Peaks in $\boldsymbol{\mathcal{L}}_{12}$ following sunspot area curvature suggest bottom-up energy injection, whereas preceding peaks may indicate top-down magnetic stress propagation.

Cross-Laplacian analysis also reveals hemispheric asymmetries in amplitude and phase across Cycles 21–25, tracking variations in flux emergence efficiency, meridional flow, and magnetic helicity between hemispheres. Enhanced $\boldsymbol{\mathcal{L}}_{12}$ in one hemisphere suggests earlier or stronger photosphere-corona coupling, consistent with known north-south dynamo asymmetries.

Laplacian analysis allows us to identify the spatial regions with the highest probability of S-flare events; the time dimension is equally important for prediction. Table 3 provides a comprehensive overview and summary of the meaning of the gradient, Laplacian, and cross-Laplacian values, as well as their mathematical and physical significance in S-flare forecasting. To find the temporal periodicities that modulate the occurrence of these events, we perform a wavelet spectral analysis to the S-flare time series in the following section.

4.10. Spectral Wavelet Analysis of S-Flare Activity Record

After analyzing the cross-Laplacian of the sunspot area and the SXR flares, we determined that S-class flares preferentially occur in areas where the Laplacian is negative because these are sink zones where magnetic flux converges or magnetic reconnection occurs. Now, we will perform a time-frequency wavelet spectral analysis to find temporal patterns that provide information about the reference occurrence of these flares over time. Wavelet analysis was performed using software based on the Torrence and Compo (1998) algorithm. Furthermore, the significance level in the global wavelet spectrum is calculated with a red-noise model (Gilman et al., 1963).

Figures 6a–6c presents the wavelet spectral analysis of the full-solar disk, northern and southern hemispheres, respectively, with signals associated with the 37 S-class flares summarized in Table 2, spanning the period from 1978 to 2025. In all these three cases, the top panel displays the time series, the left panel displays the global wavelet spectrum, and the middle panel displays the wavelet power spectral density (PSD).

These S-flares are analyzed as a digital signal (Equation 1) and these events are indicated by black, blue, and red bars in the upper panel of Figures 6a–6c, respectively. To facilitate visualization, the southern hemisphere S-flare events are shown with an inverted scale. We may note that the digital signal processing methodology has been

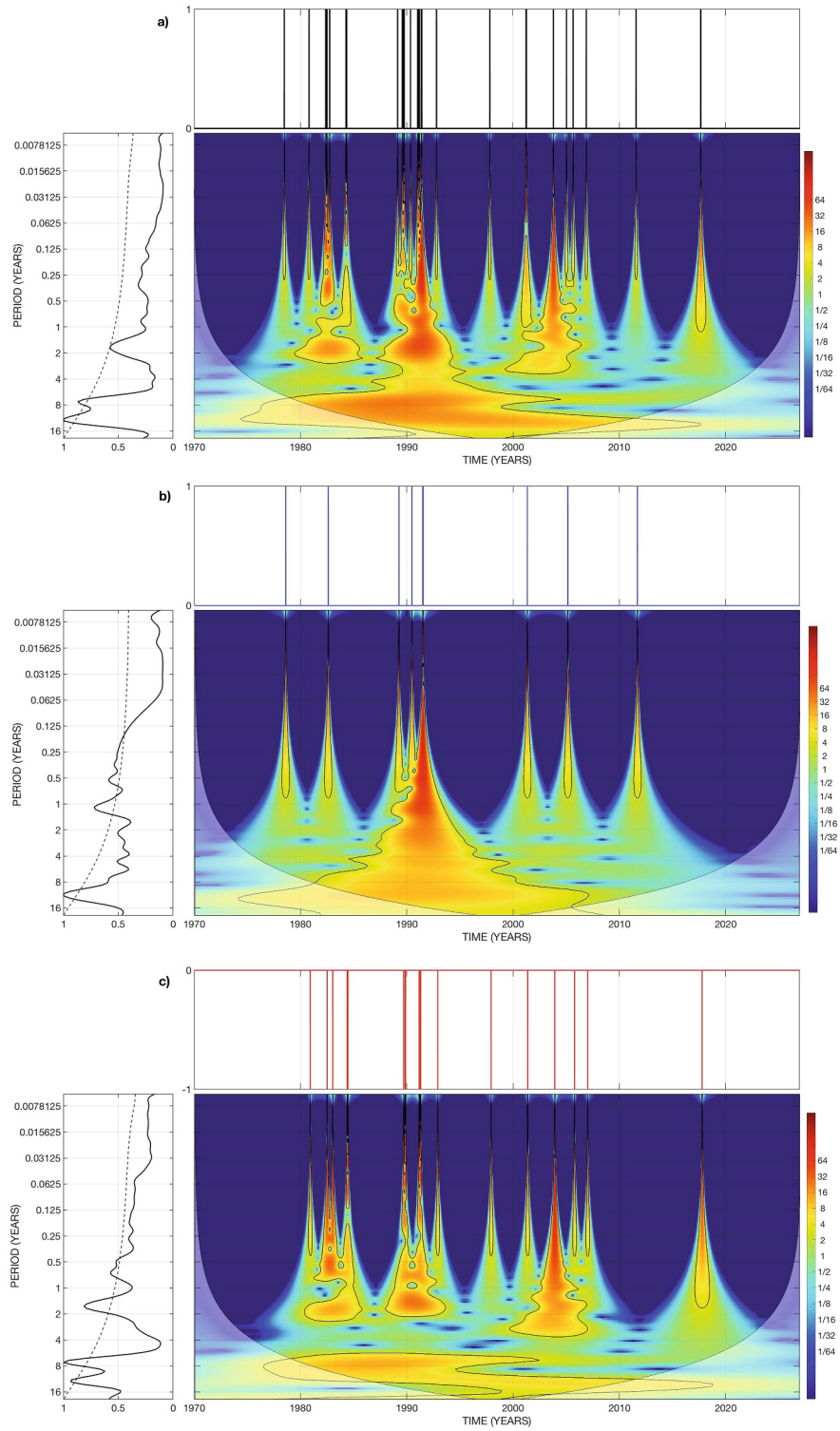

Figure 6. Time-frequency wavelet results of the S-flare events: (a) Full solar disk (black bars), (b) Northern hemisphere (blue bars), and (c) Southern hemisphere (red bars) of the solar corona. In these three cases, the S-flare time series is displayed in the top panel. The left panel shows the global wavelet spectrum. Finally, the central panel displays the wavelet power spectral density (PSD) in normalized units adopting the red-green-blue (from the highest to lowest power) color scales. The cone of influence (COI, U-shaped curve with shaded outer zones) shows the possible edge effects in the PSD. The significance level in the global wavelet spectrum is calculated with a red-noise model and its shown as dotted black line.

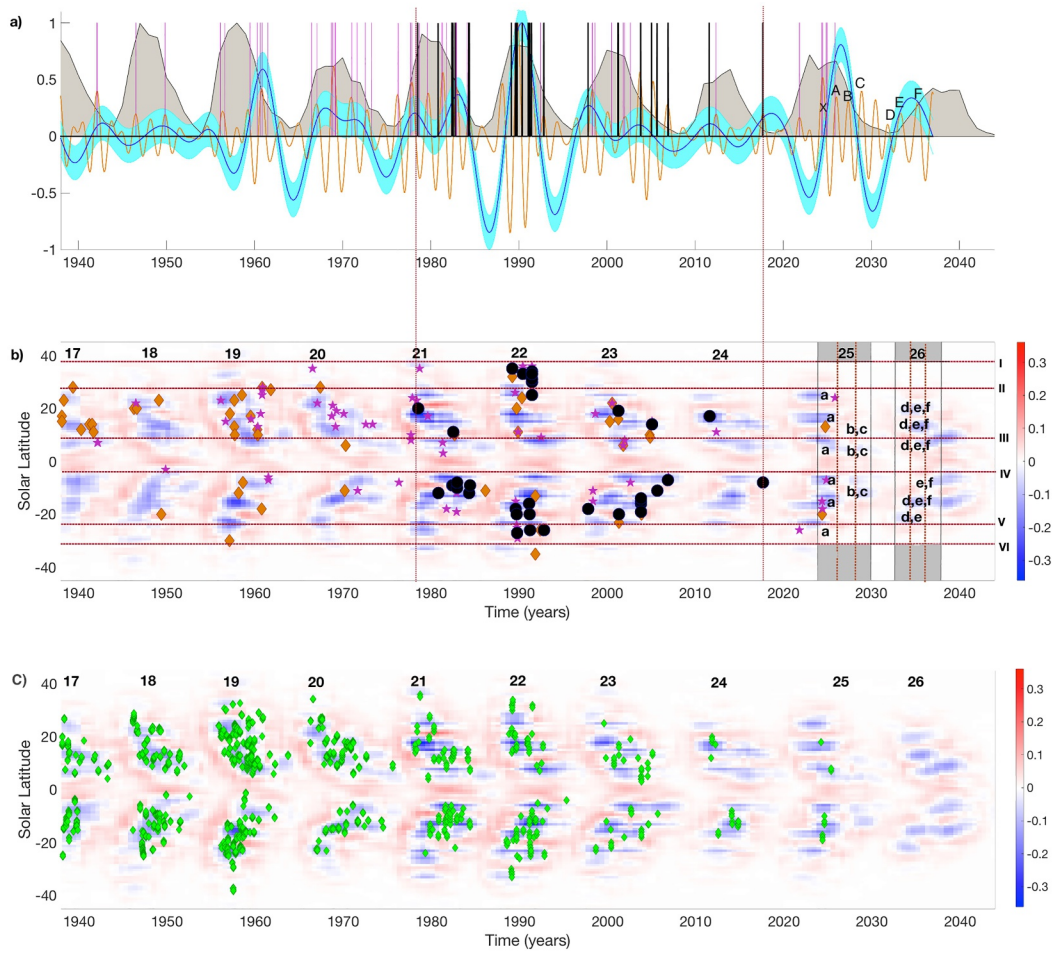

Figure 7. Integrated spatiotemporal forecast for S-class flares in Solar Cycles 25 and 26. (a) *Temporal forecast:* The coupled-phase model of the 1.7-year (orange) and 7-year (cyan) oscillations identifies high-probability windows (labeled A–F) for extreme solar activity. The label X marks the two newly identified S-class flares, X11.1 and X 16.5, on 14 May and 20 May 2024, respectively, by the Solar Orbiter Mission as reported recently by Stiefel et al. (2025) and Kontogiannis et al. (2025). Historical S-class flares (black vertical lines) and Ground Level Enhancement (GLE) events (purple vertical lines) are shown for validation. Gray shading represents the annual sunspot number for context. (b) *Spatial forecast:* Extended and projected Laplacian map of sunspot area distribution (1938–2044), where blue regions indicate negative Laplacian (magnetic energy accumulation zones). Historical S-flares (black dots), GLE events (purple stars), and intense geomagnetic storms (< -250 nT; orange diamonds) are superimposed. Brown dotted lines mark recurrent preferential latitudinal bands. Lowercase letters (a)–(f) denote the high-risk spatial zones corresponding to the temporal windows in panel (a). The superposition of these labels (A–a, B–b, etc.) defines the spatiotemporal domains of maximum probability for S-class flare occurrence in Cycles 25 and 26, providing a unified probabilistic forecast with ∼1-year temporal and ∼10° latitudinal resolution. (c) Green diamonds indicate the location of sunspot clusters with an area >1200 μHm.

employed by us to investigate periodicities in both GLE events (see Velasco Herrera et al., 2018) and other abrupt phenomena previously, so this methodology can be applied to analyze the S-class flares as well.

The global wavelet spectrum of the full-solar disk in the left panel of Figure 6a reveals three dominant periodicities exceeding the 95% confidence level with significant spectral power: 11.5 ± 3 years, 7.3 ± 1 years, and 1.7 ± 0.2 years. Additionally, there are other periodicities with less than 95% reliability, but they will not be discussed and further analyzed in this work because they are not necessary to the forecasting method and result performed in this paper. The uncertainty is quantify from the half maximum of the peak of each periodicity shown in the global wavelet (Mendoza et al., 2006).

The 11.5-year periodicity corresponds to the well-established solar cycle (Schwabe, 1844), indicating that S-class flare occurrence is modulated by fundamental photospheric magnetic activity. The 1.7-year periodicity has been

previously documented in GLE events, cosmic ray variations, and various solar activity indices (Korsós et al., 2023; Stefani et al., 2025; V. M. Velasco Herrera et al., 2018). Furthermore, Deng et al. (2019) and Korsós et al. (2023) demonstrate that statistically significant enhancements in solar Hα flare and M- and X-class solar flare occurrence are associated with a persistent ∼1.7 years periodicity, respectively. Korsós et al. (2023) and Stefani et al. (2025) indicate for the fundamental role of the 1.7-year oscillation in the synchronization to linking associations among various solar activity timescales. Additionally, it is suggested that, this periodicity are resulting from tidally triggered magneto-Rossby wave at the tachocline (Korsós et al., 2023; Stefani et al., 2025).

Analyzing hemispheric S-flares with the wavelet transform, the northern hemisphere result (Figure 6b) yields significant periodicities at 11.5, 7.3, and 2.1 years, whereas the southern hemisphere result (Figure 6c) exhibits corresponding periodicities at 11.6, 7.3, and 1.6 years. The primary distinction in the hemispheric S-flare dynamics lies in the mid-term periodicities (MTP Mendoza et al., 2006), specifically in oscillations within the 1–2 years. This hemispheric asymmetry in solar flare activity for MTP, has been previously reported by Mendoza and Velasco Herrera (2011) for Solar Cycles 21–23 and by V. Velasco Herrera et al. (2025) for Solar Cycles 17–25.

The SFI and H-α shows an odd–even pattern and this activity in the northern hemisphere begins earlier than that in the southern hemisphere, with phase shifts ranging within several months (Deng, Qu, et al., 2013; Deng, Gai, et al., 2013; Deng et al., 2019; V. Velasco Herrera et al., 2025). The odd-even pattern is the equivalent of the Gnevyshev-Ohl rule for solar flare activity in the solar chromosphere, while the phase shift in hemispheric chromospheric solar activity forms the Gnevyshev gap observed at the solar maximum of a solar cycle, showing two peaks in amplitude with a gap between these twin peaks of one to 2 years (V. Velasco Herrera et al., 2025).

One of the main observational differences in chromospheric and coronal asymmetry lies in the shift of the 1.7-year periodicity of the full solar disk. Wavelet analysis of the Northern Hemisphere of the SFI shows periodicities of 1.4 years. However, in the Southern Hemisphere, the equivalent periodicity is 1.8 years (V. Velasco Herrera et al., 2025). Meanwhile, in the case of S-flares, the 1.7-year periodicity changes to 2.1 and 1.6 years for the Northern and Southern Hemispheres, respectively. This difference between the solar corona and chromosphere has to be further studied both theoretically and with solar dynamo simulations

The 7.3-year periodicity (L. I. Miroshnichenko et al., 2012), while reported in GLE events, appears less prevalent in general solar indices, suggesting it may be specifically or exclusively associated with explosive solar phenomena. This periodicity does not corresponds to any known harmonics of the main solar cycle of 11-year and therefore requires an alternative physical explanation.

Rossby waves (Rossby, 1939), have been increasingly recognized as important agents in solar magnetohydrodynamics. Theoretical models predict the existence of multiple magneto-Rossby wave modes in the solar convection zone (see, e.g., Dikpati & McIntosh, 2020; Zaqarashvili et al., 2007) with periods clustered around 1–2 years and we propose that the observed ∼7-year periodicity arises from the beating (interference) between two such magneto-Rossby modes with closely spaced periodicities.

We propose that the ∼7-year periodicity observed in S-flare records can be explained as a beat frequency resulting from the superposition of two magneto-Rossby modes with nearby intrinsic periods. Consider two modes with periods T_1 and T_2. The beat period (see e.g., Stefani et al., 2025) is given by:

$$\frac{1}{T_{\text{beat}}} = \left|\frac{1}{T_1} - \frac{1}{T_2}\right|, \tag{3}$$

This beating produces a long-term amplitude modulation of the shorter-period oscillations, effectively creating an envelope with the beat period. For the specific case of $T_1 = 1.7$ year and $T_2 = 1.4$ year, the beat period $T_{\text{beat}} = 7.9$ year can be deduced. This value roughly matches the observed ∼7-year periodicity within measurement uncertainties. Importantly, both T_1 and T_2 lie within the uncertainty band of the well-established ∼1.7-year oscillations detected from flare activity records based on the full solar disk as well as the hemisphere-resolved solar corona and chromosphere.

The physical mechanism involves the nonlinear interactions of these magneto-Rossby modes with the solar dynamo. The amplitude modulation generated by the frequency beating can enhance or suppress the emergence of S-flare productivity on multiannual timescales. The coupling of such modes can produce amplitude modulations

that naturally explain long-term variations without requiring additional oscillatory components in the dynamo itself. Therefore, we suggested, that this periodicity does not require an additional oscillator independent of the solar dynamo, but instead can be generated by the beating between magneto-Rossby wave modes with closely spaced periods. This mechanism modulates the occurrence rate of S-flares by creating alternating periods of enhanced and suppressed magnetic activity on ∼7-year timescales. Another alternative physical interpretation could explain the ∼7-year periodicity as the third harmonics of the main magnetic cycle of 22-year (i.e., the Hale cycle, see e.g., Gailitis et al., 2018).

The temporal evolution of these periodicities is shown as PSD in the middle panel (see especially Figure 6c for the Southern Hemisphere S-flares). Both the solar cycle and 7.3-year periodicities persist throughout the entire observational chromospheric SFI record from 1937 to 2025 as well (not shown directly in Figure 6a but can be seen in V. Velasco Herrera et al., 2025). The spectral power of the solar cycle periodicity peaks between 1978 and 2017, while the 7.3-year periodicity exhibits maximum strength during the whole 1937–2003 interval.

The latitudinal organization of sunspot emergence is primarily governed by the ∼11-year cycle, evident as the equatorward migration of activity belts in the butterfly diagram. This pattern is closely linked to the amplification and storage of the toroidal magnetic field in the tachocline. The dominant longitudinal periodicity is the solar rotation of approximately 27 days (Kane, 2002), modified by latitude-dependent differential rotation. Persistent longitudinal structures, such as ALs, sunspot nests, and flare clusters, rotate with the local flow, imprinting a strong ∼27-day modulation on flare productivity.

Beyond the well-known rotational (∼27 days) and solar cycle (∼11-year) periodicities, solar magnetic activity exhibits a distinct modulation with periods of approximately 1–2 years. This quasi-biennial oscillation (QBO) manifests across multiple solar indices—including sunspot number, sunspot area, flare occurrence, torsional oscillations, and helioseismic diagnostics of internal rotation (Benevolenskaya, 1995, 1996; McIntosh et al., 2015). The butterfly diagram, which tracks the latitudinal distribution of magnetic emergence, reveals small-scale undulations superposed on the gradual equatorward drift of active regions. Wavelet and spectral analyses of long-term sunspot catalogs indicate that these latitudinal modulations occur with characteristic periods of $P \approx 1.3$–1.8 years. These oscillations appear as episodic variations in the drift rate, alongside bursts of enhanced emergence at specific latitudes in both hemispheres.

Active Longitudes (ALs), persistent longitudinal sectors with heightened magnetic emergence, also display quasi-biennial variations. Studies using sunspot records show that the longitudinal clustering of solar activity fluctuates over 1–2 years timescales (Gyenge et al., 2016; McIntosh et al., 2014). The quasi-biennial oscillation (QBO) exchanges the intensity of AL in a more defined and strong way; alternating with weak phases, so that AL becomes more diffuse (Berdyugina & Usoskin, 2003; Moss, 1999). The detailed recent analyses by Korsós and Erdélyi (2025) also confirmed the presence of various QBO-scale oscillations in their study of distribution of magnetically complex active regions and energetic solar flares. These authors found that during solar minimum between Cycles 23 and 24, ALs clustered around 200° longitude for nearly 3 years. The concurrent presence of QBO in both latitude and longitude indicates that these periodicities is a global feature of solar magnetic activity. Furthermore, the QBO manifests as synchronized enhancements in active-region emergence at specific latitudes and longitudes, along with modulated flare productivity and coronal heating (Huang et al., 2025; McIntosh et al., 2015). The solar QBO represents a fundamental intermediate-timescale modulation that influences both the latitudinal migration of activity belts and the longitudinal clustering of magnetic emergence.

The 1.7-year periodicity (QBO) likely has both a heliographic latitudinal origin and a temporal component, suggesting that S-class flares may be modulated by this oscillation. In addition, the 7-year periodicity may also be synchronized with the occurrences of these flares. For this reason, we use these two periodicities to construct a temporal clustering, which serves as the basis for forecasting S-class flare occurrences in the coming years.

4.11. Temporal Forecasting of S-Class Flares Using Machine Learning

Building upon the spatial patterns identified through gradient and Laplacian analyses of the SXR flare butterfly diagram (Sections 4.2–4.7), we now develop a temporal forecasting framework for S-class flares. Unlike conventional flare prediction approaches that target individual events on short timescales, our methodology identifies extended temporal windows with enhanced probability for extreme flare occurrence, operating on medium to long-term horizons.

Table 4
Historical List of Solar Events With GLE, SFI, Soft X-ray (SXR), Importance (Hα/X), and Latitude (Hα Position)

Year	Month	DAY	GLE	I	SFI	SXR	LAT
1942	02	28	01	3+	34.78		N07
1942	03	07	02				N07
1946	07	25	03	3+			N22
1949	11	19	04	3+	18.46		S03
1956	02	23	05	3	1.83		N23
1956	08	31	06	3	53.91		N15
1959	07	17	07	3+	18.99		N16
1960	05	04	08	2	10.84		N13
1960	09	03	09	2+	18.12		N18
1960	11	12	10	3+	58.12		N27
1960	11	15	11	3+	24.33		N25
1960	11	20	12	2	15.99		N28
1961	07	18	13	3+	30.00		S07
1961	07	20	14	3	17.45		S06
1966	07	07	15	2B	20.33		N35
1967	01	28	16		4.96		N22
1967	01	28	17		4.96		N22
1968	09	29	18	2B	17.71		N17
1968	11	18	19	1B	5.13		N21
1969	02	25	20	2B	22.42	X2.0	N13
1969	03	30	21	1N	5.08		N19
1970	01	24	22	3B	0.98	X5.0	N18
1971	09	01	23		0.17		S11
1972	08	04	24	3B	33.95	X4.0	N14
1972	08	07	25	3B	35.25	X4.0	N14
1973	04	29	26	2B	22.29	X1.0	N14
1976	04	30	27	1B	5.42		S08
1977	09	19	28	3B	22.04	X2.0	N08
1977	09	24	29		3.16		N10
1977	11	22	30	2B	15.52	X1.0	N24
1978	05	07	31	2B	8.97	X1.0	N23
1978	09	23	32	3B	28.62	X1.0	N35
1979	08	21	33	2B	31.27		N17
1981	04	10	34	2B	63.00	X2.3	N07
1981	05	10	35	1N	10.92		N03
1981	10	12	36	2B	37.90	X3.1	S18
1982	11	26	37	1N	13.21		S12
1982	12	07	38	1B	35.19	X2.8	S19
1984	02	16	39	1N	2.16		S16
1989	07	25	40	1B	4.80		N26
1989	08	16	41	2N	18.35		S15
1989	09	29	42	1B	19.53	X9.0	S24

The temporal foundation of our forecast derives from wavelet spectral analysis (Section 4.8), which reveals two dominant periodicities modulating S-flare occurrence: ∼1.7-year and ∼7-year cycles (V. M. Velasco Herrera et al., 2018; V. Velasco Herrera et al., 2025). We propose that these extreme events require constructive interference between both oscillatory modes, specifically manifesting only during simultaneous positive-phase intervals.

To implement our new forecasting framework and concept, we use the algorithm that combines Bayesian ML and wavelet analysis with Least-Squares Support Vector Machines (LS-SVM, see Suykens et al., 2005, for more detail on the method). Furthermore, we use the radial basis function kernel and the *K*-fold cross-validation for the training, validation, testing, and deduction of the parameters of the LS-SVM (see V. Velasco Herrera et al., 2021; V. Velasco Herrera et al., 2025, for more detail on the algorithm).

Our methodology deliberately excludes the 37 known S-flare events (Figure 1, Table 2) from training to prevent overfitting. Our goal is not to predict individual flares, but to forecast *the most probable time windows* for their occurrence. Drawing on experience from aurora forecasting (V. Velasco Herrera et al., 2025), we train a LS-SVM model using the 1.7- and 7-year solar oscillations derived from wavelet analysis for 1978–2017 (Figure 6). This interval, marked by two vertical brown dotted lines across both panels (a) and (b), is split into a training period (1978–2008) and a verification period (2008–2017).

The trained model first reconstructs both oscillations back to 1938 (left of the first vertical brown dotted line at 1978 in Figure 7). This reconstruction is validated against the first 30 GLE events (Table 4), all of which fall within the positive phase of the 1.7-year oscillation, consistent with earlier findings (V. M. Velasco Herrera et al., 2018). The model then forecasts S-flare windows beyond 2017 (right of the second vertical brown dotted line at 2017 in Figure 7). Its ability to replicate the occurrence of events GLE for 73 to 77, that occurred exclusively in positive phases further validates the approach.

We finally extend the forecast to 2044, covering the ascending phase of Solar Cycle 26. For visual clarity, only the 7-year oscillation is shown in the projection, with blue shading representing the 95% confidence interval from the Bayesian model; the 1.7-year oscillation confidence intervals are omitted. The LS-SVM model thus extracts and projects the phase states of both cycles, producing physically interpretable signals for flare-window prediction.

The forecasting strategy employs a risk classification: periods are designated as high-probability windows for S-flare activity if, and only if, both oscillations are predicted to be in simultaneous positive phases. This approach anchors predictions directly in the physical state of the oscillatory system, circumventing well-known challenges in probability calibration for rare events while maintaining physical interpretability.

Ensemble analysis incorporating 1000 realizations for each periodicity confirmed that temporal phase variations, rather than amplitude changes, provide the most critical forecasting information. The resulting model demonstrates that S-class flares occur preferentially during positive phases of the 1.7-year oscillation–a pattern previously identified for GLE events and severe geomagnetic storms (V. M. Velasco Herrera et al., 2018; V. Velasco Herrera et al., 2025).

Table 4
Continued

Year	Month	DAY	GLE	I	SFI	SXR	LAT
1989	10	19	43	3B	88.96		S25
1989	10	22	44	1N	41.48		S27
1989	10	24	45	2N	39.68		S29
1989	11	15	46	2B	52.07		N11
1990	05	21	47	2B	36.71		N34
1990	05	24	48	1B	12.00		N36
1990	05	26	49		10.02		N35
1990	05	28	50		4.06		N35
1991	06	11	51	2B	37.54	X12.0	N32
1991	06	15	52	2B	40.21	X12.0	N36
1992	06	25	53	2B	27.31		N09
1992	11	02	54		13.70	X9.0	S25
1997	11	06	55	2B	11.30	X9.4	S18
1998	05	02	56	3B	28.59	X1.1	S15
1998	05	06	57	1N	20.22	X2.7	S11
1998	08	24	58	3B	34.06	M7.1	N18
2000	07	14	59	3B	59.13	X5.7	N22
2001	04	15	60	2B	13.19	X14.0	S20
2001	04	18	61			C2.2	S20
2001	11	04	62	3B	75.00	X1.0	N06
2001	12	26	63	1B	50.94	M7.1	N08
2002	08	24	64	1F	10.54	X3.1	S08
2003	10	28	65	4B	144.32	X17.0	S16
2003	10	29	66	2B	31.87	X10.0	S15
2003	11	02	67	2B	30.47	X8.3	S14
2005	01	17	68	3B	33.60	X3.8	N15
2005	01	20	69	2B	23.75	X7.1	N14
2006	12	13	70	4B	47.55	X3.4	S06
2012	05	17	71	1F	4.17	M5.1	N11
2017	09	10	72			X8.2	S08
2021	10	28	73		8.88	X1.0	S26
2024	05	11	74		38.42	X5.8	S15
2024	06	08	75		4.88	M9.7	S18
2024	11	21	76		0.88	C5.9	S07
2025	11	11	77		1.10	X5.1	N24

Remarkably, application of this phase-coupling framework to the complete historical record of GLE events provides a confident and robust validation (L. Miroshnichenko, 2015; Le & Liu, 2020). All 77 GLEs recorded between 1942 and 2025 (see Table 4) occur exclusively during coupled positive-phase windows (Figure 7a). The consistent coincidence of GLE events with positive oscillation phases, extending back to 1942, strongly suggests that S-class flares similarly occurred during these historical positive-phase windows prior to the GOES era (pre-1975). Particularly notable events such as the February 1942 GLE and July 1946 GLE—occurring decades before systematic X-ray monitoring—align perfectly with positive-phase intervals identified by our reconstruction. Furthermore, such a notable correlation, spanning eight solar cycles and encompassing a different class of eruptive phenomenon, provides compelling evidence that the phase-coupling mechanism captures a fundamental property of extreme solar activity.

However, the 1.7-year oscillation alone represents a necessary but insufficient condition. Both GLEs and S-class flares occur exclusively during simultaneous positive phases of both oscillations, indicating that constructive interference across multiple temporal scales is required for manifestation of extreme superflare events.

Application of this validated model to Solar Cycles 25 and 26 identifies six high-probability intervals (labeled A–F in Figure 7a). For Cycle 25, the forecasted high-risk periods are:

- *Point A:* 2025.7 ± 0.2 years–2026.6 ± 0.2 years
- *Point B:* 2027.2 ± 0.2 years–2027.9 ± 0.2 years
- *Point C:* 2028.8 ± 0.2 years–2029.7 ± 0.2 years

Furthermore, for Cycle 26, the forecasted high-risk periods are

- *Point D:* 2030.6 ± 0.2 years–2031.5 ± 0.2 years
- *Point E:* 2032.3 ± 0.2 years–2033.2 ± 0.2 years
- *Point F:* 2034.1 ± 0.2 years–2034.9 ± 0.2 years

The integration of this temporal forecast with spatial diagnostics based on negative Laplacian regions (Figure 7b) establishes the first comprehensive spatiotemporal probabilistic framework for S-class flares. This unified approach enables identification of not only when but also where these extreme events are most likely to occur, providing actionable forecasting information with long lead times of year to multi-years.

Classical solar flare forecasting relies on the P. McIntosh classification of sunspot groups. The McIntosh classification remains a foundational tool for operational forecasting. By calculating average flare rates for each class, forecasters can determine Poisson probabilities for flares of different magnitudes (Bloomfield et al., 2012). A recent analysis recalculated these rates, finding a significant increase for M- and *X*-class events after accounting for the GOES/XRS rescaling (Janssens et al., 2025). This work confirmed the system's efficacy in distinguishing flare-active from flare-quiet regions, highlighting that nearly half of all major flares are produced by a small fraction (~8%) of complex sunspot groups.

Furthermore, flaring potential exhibits significant variation across the solar cycle. An analysis of Solar Cycles 23 and 24 revealed that the largest and most complex sunspot groups (McIntosh's sunspot classes *D*, *E*, and *F*) produced nearly 80% of all flares, with the highest flaring potential often occurring during the cycle's descending phase (Singh et al., 2024).

Early ML efforts demonstrated the predictive power of features derived from vector magnetic field data. Bobra & Couvidat, 2015 used a SVM trained on 25 parameters from SDO/HMI vector magnetograms to forecast M- and

X-class flares, achieving high True Skill Statistic (TSS) scores. This indicated that a compact set of physical parameters could yield strong predictive performance.

More recent work leverages Deep Learning to automatically extract complex features directly from data. Hybrid architectures, such as a Convolutional Neural Network combined with a Temporal Convolutional Network, have been developed to predict ≥C- and ≥M-class flares (Xu et al., 2025). These models fuse spatial structure from images with the temporal evolution of magnetic fields, achieving high average TSS scores (e.g., 0.798 for ≥C-class and 0.850 for ≥M-class flares). This high performance suggests the models are identifying physically significant features beyond those defined by traditional analysis.

Both the classical McIntosh classification and modern ML techniques provide valuable insights for flare forecasting. While the former offers a physically interpretable framework, the latter, particularly by applying Deep Learning algorithm, excels at identifying complex, non-linear patterns in high-dimensional data, pushing the boundaries of predictive capability.

The comprehensive analysis presented herein reveals that Solar Cycle 24, while exhibiting relatively low overall activity, likely accumulated significant magnetic energy that remained stored within the solar atmosphere. Our model suggests that the Sun may now release this accumulated energy during Solar Cycle 25, manifesting as abrupt, highly energetic events including GLEs, S-class flares, and potentially associated CMEs. This energy release scenario aligns with both the temporal forecasting derived from coupled oscillations and the spatial patterns identified through cross-Laplacian analysis, which indicate the development of magnetic energy reservoirs during any individual solar activity cycle.

4.12. Probabilistic Latitudinal Forecast of S-Class Flares

Having established the temporal forecasts using the LS-SVM model, we now complement it with the *spatial component* to identify the latitudes most likely to produce S-class flares in the coming years.

As demonstrated in Sections 4.5, 4.6 and 4.7, Laplacian analyses of both the sunspot butterfly diagram and SXR flare distribution reveals that S-class flares preferentially cluster in regions of negative Laplacian (blue regions in Figures 5a and 5c). These negative-curvature regions correspond to *latitudinal zones of enhanced magnetic energy accumulation*, where the largest sunspot groups (area >1200 μHem) preferentially develop and serve as source regions for extreme flare events.

To extend this analysis, we constructed an extended Laplacian map of the sunspot-area distribution dating back to 1938 in parallel to the temporal analysis performed for GLEs and our SFI activity record. Superimposing the locations of sunspot groups with area >1200 μHem (green diamonds in Figure 7c) onto this Laplacian map demonstrates that the most active regions consistently form within or adjacent to negative-Laplacian structures. When these spatial concentrations are combined with the phase-aligned temporal windows of enhanced flare probability (Figure 7a), they naturally define *spatiotemporal intervals of elevated risk*. Notably, the GLEs cataloged in Table 4 also localize within these super-active regions, closely mirroring the behavior of S-class flares.

The extended Laplacian analysis, applied from 1938 onward, further enables the reconstruction of epochs and latitudes where S-class flares likely occurred, even prior to the availability of direct SXR observations. The resulting Laplacian map reveals distinct and recurrent preferential latitudinal bands in each hemisphere where regions of negative curvature systematically emerge.

These bands, indicated by horizontal brown dotted lines in Figure 7b, are evidently non-random. In the northern hemisphere, negative-Laplacian structures cluster near latitudes of approximately 30° and 10°, whereas in the southern hemisphere they concentrate around 5° and 25°. These latitudinal zones are delimited by labels with Roman numerals II–III and IV–V, respectively. Additionally, two secondary latitudinal sub-bands correspond to historical locations of S-class flares during solar cycle 22: one between 40° and 30° north, and another between 25° and 35° south. These sub-bands are similarly bounded by brown dotted lines and marked with Roman numerals I–II and V–VI, respectively.

Additionally in Figure 7b, black dots indicate the latitudinal location of historical S-class flares (Table 2) and the active regions that are the sources of the 77 GLE events (Table 4) as purple stars, and geomagnetic storms < -250 nT in orange diamonds. Geomagnetic storms and GLE events also occur only in the positive phase of

the 1.7-year oscillation (V. M. Velasco Herrera et al., 2018; V. Velasco Herrera et al., 2025). All these events are grouped in the blue areas that correspond to the negative values of the Laplacian.

Statistical analysis of extreme flares (1976–2018) reveals that all ≥X5 events were confined to latitudes between 30°S and 35°N (Li et al., 2024). Most occurred within a 5-year window centered on solar maximum, from 2 years before to 3 years after the peak. Significant North–South asymmetry was observed, with the southeastern quadrant exhibiting the highest flare activity.

Flare-productive active regions typically host strong magnetic non-potentiality, often manifesting as δ-sunspots and sheared polarity inversion lines (Toriumi & Wang, 2019). The underlying physical mechanism involves accumulation and subsequent release of magnetic energy through reconnection.

Solar flare forecasting is advancing rapidly, driven by both high-quality observational data and sophisticated ML algorithms. Meanwhile the McIntosh-based statistical methods provide a valuable baseline, superior predictive performance may comes from Deep Learning models employing vector magnetic field data.

Currently, no established method exists for forecasting the sunspot emergence butterfly diagram. We therefore adopt the following approach: Using a Monte Carlo technique, we generated 1000 realizations of synthetic butterfly diagrams for Solar Cycles 17–24. From these synthetic diagrams, we extracted the average spatio-temporal evolution after the first five years of the start of each solar cycle—an interval chosen to match the current observational extent of Solar Cycle 25. This averaged pattern was then used to construct a complete synthetic butterfly diagram for the full Cycle 25. Repeating this procedure for Cycles 17–25 produced another ensemble of 1000 synthetic diagrams, then we adopted the mean pattern for Solar Cycle 26 under the assumption of an average cycle duration of ∼11 years and persistence of historical latitudinal emergence patterns.

The resulting forecast is shown in Figure 7b, to the right of the first vertical line around November 2025. Negative-Laplacian regions (blue areas) extend smoothly from November 2025 into the projected portion without abrupt discontinuities, suggesting that latitudinal evolution across Cycle 25's ascending phase and into Cycle 26 remains consistent with historical patterns. Furthermore, these blue regions maintain alignment with the preferential latitudinal bands, indicating that the Monte Carlo-generated synthetic butterfly diagrams successfully reproduce characteristic sunspot emergence spatial structure.

Integration of the detailed spatial information with the temporal forecast is accomplished by superimposing the positive-phase windows of the 1.7-year oscillation (labeled A–F in Figure 7a) onto the projected Laplacian map. The corresponding lowercase identifiers (a–f) in Figure 7b thus delineate the spatiotemporal intervals of greatest likelihood, where the requisite large-scale physical state negative Laplacian, indicative of magnetic energy accumulation, that coincides with the high probability temporal phases of the oscillation.

For Solar Cycles 25 and 26, we therefore anticipate that S-class flares are most likely to originate at mid-latitudes situated between the primary northern and southern bands, predominantly within the negative-Laplacian regions (blue areas labeled a–f). In contrast, flare occurrence is expected to be less frequent at the higher-latitude zones bounded by the secondary bands in Figure 7b.

In the new framework introduced in this paper, the Laplacian serves as the spatial complement to the wavelet-based temporal forecast, providing a physically motivated indicator of where extreme solar activity is most likely to occur. We emphasize that the projected Laplacian depends on the model used to extend the sunspot area distribution beyond the present epoch. Therefore, spatial patterns shown for 2025–2044 should be strictly interpreted as probabilistic structures rather than deterministic predictions. Nevertheless, the historical coherence between negative Laplacian regions and major events suggests this diagnostic retains physical meaning even when extended into the forecast regime. Combined with the phase-coupled temporal analysis of Figure 6a, this integrated framework provides a powerful tool for identifying the most probable locations of future S-class flares through ∼2044.

The superposition of the temporal windows (A–F) with the negative Laplacian spatial bands (a–f) defines the spatiotemporal domains of maximum risk for the occurrence of S-flares in Cycles 25 and 26. This approach provides advanced a new short- and long-term early warning system with a resolution of ∼1 year and ∼10° in latitude, allowing for focused preparation for future extreme space weather events.

To facilitate operational interpretation of our probabilistic forecast, Table 5 summarizes the identified high-probability and medium-probability windows for Cycles 25 and 26. The qualitative probability is based on the amplitude and phase coherence of the 1.7-year and 7-year oscillations, as well as the robustness of the projected negative Laplacian structures:

- *High Probability:* Assigned when the window exhibits (a) strong simultaneous positive phase in both oscillations (1.7-year and 7-year), (b) overlap with a well-defined negative Laplacian band in the projection, and (c) historical analogy with periods of multiple S-flares/GLEs.
- *Medium Probability:* Assigned when the coupled-phase criterion is met, but the negative Laplacian signal is less defined or the latitudinal band is secondary.
- Latitudinal bands are approximate, based on the historical location of negative Laplacian regions and the expected migration of the butterfly diagram. The southern hemisphere shows stronger structure in Cycle 25, while the northern hemisphere may gain predominance in Cycle 26.
- Temporal uncertainty (±0.2 years) reflects the full width at half maximum in the wavelet spectrum of the modulating oscillations.

The integration of temporal and spatial forecasts establishes an operational framework for S-class flare prediction, enabling identification of both the timing and locations of highest risk. This unified approach provides actionable forecasting information with lead times of years, suggesting that entry into coupled positive-phase windows should trigger enhanced monitoring campaigns using short-term prediction algorithms.

The anticipated increase in S-class flare activity during Cycle 25–statistically expecting between 3 and 8 events compared to only three in Cycle 24–underscores the importance of this advance warning system. By maintaining physical interpretability through coupled oscillation analysis and Laplacian spatial diagnostics, this comprehensive spatiotemporal framework offers a robust foundation for operational space weather forecasting throughout Cycle 25 and into the onset of Cycle 26.

It would be highly beneficial for our spatiotemporal forecasting framework to be complemented by operational prediction methods that provide hourly or daily resolution. In particular, the time–latitude coordinates (A-a, B-b, … , F-f) identified in Figure 7 as high-probability windows may offer a useful context in which even shorter-term forecasts can be further refined.

In addition, to assess the performance of our method and quantify its false-alarm rate–that is, to determine how many of the high-probability windows (A-a, B-b, … , F-f) do not yield an S-class flare–it will be necessary to evaluate the detection probability and the false-positive rate once Solar Cycle 25 has concluded. Such an assessment will provide a more complete characterization of the predictive skill of the proposed approach and enable comparison with other forecasting techniques.

We emphasize that, according to our analysis, the occurrence of an S-class flare requires a very specific local magnetic configuration, whereas the latitudinal and spatial conditions are provided in a probabilistic sense. Our model identifies spatiotemporal regions in both solar hemispheres that are favorable for the formation and development of such events.

Following the first (anticipated) S-class flare of Solar Cycle 25, additional information will become available that will allow a more precise characterization of the spatiotemporal conditions under which these flares emerge. This, in turn, will enable us to refine and optimize our space-weather forecasting capabilities for severe events.

Additionally, within the blue zones identified for Solar Cycles 25 and 26 shown in Figure 7, not only S-class flares but also GLEs, unusually large sunspot groups, and intense geomagnetic storms are expected to be highly probable. These associations are grounded in phenomenological patterns observed across Solar Cycles 17–25, suggesting that the present framework can be extended to forecast multiple space-weather manifestations. Such capability would mark a shift from reactive mitigation to proactive planning years in advance, representing a significant change in how we prepare for severe solar events that can disrupt both space- and ground-based technological systems.

As our forecast product provides multi-year spatiotemporal risk zones rather than point-wise probabilistic values, full verification of predictive skill necessarily requires to wait until the completion of Solar Cycle 25. Only once the cycle concludes will it be possible to compute zone-level performance metrics such as spatial-temporal coverage, hit fractions, intersection-over-union between predicted and observed zones, and displacement

statistics for the predicted bands. These metrics depend on the actual future occurrence of S-class flares, GLEs, and related extreme phenomena like intense geomagnetic storms within the predicted windows.

For the present study, we therefore restrict our quantitative assessment to a retrospective validation across Cycles 17–24, for which complete data are available. This hindcast demonstrates that negative cross-Laplacian structures and coupled oscillatory windows (1.7-year and 7-year phases) consistently coincide with historical extreme-event zones. However, the definitive forward validation, whether Cycle 25 events fall within the predicted zones, can only be established once this cycle ends. At that time, a full zonal verification following standard space-weather validation protocols will be performed.

As discussed in the Introduction, solar flares are routinely classified by their peak SXR flux, as measured by the GOES satellite series. A critical new capability is provided by the Spectrometer/Telescope for Imaging X-rays (STIX) aboard the Solar Orbiter mission. Due to the Solar Orbiter's heliocentric orbit, STIX observes a significant fraction of flares from the Sun's far side, which are not directly detected by Earth-orbiting GOES satellites. For these events, a cross-calibrated flux is estimated to provide an equivalent GOES-class magnitude (see Stiefel et al., 2025, for more details).

Two notable latest examples of such far-side events are the strong flares on 14 May 2024 at 05:14 UTC and 20 May 2024 at 16:47 UTC, with estimated GOES classes of X11.1±1.2 and X16.5±1.8, respectively (Kontogiannis et al., 2025; Stiefel et al., 2025). These events occurred in the area marked with an "*X*" in Figure 7a and occurred during the onset of the positive phase of concurrent 7-year and 1.7-year oscillations identified in our analysis. Their occurrences may indeed serve as an independent (since we did not even know about the existence of these two strong flare events when we were preparing our forecasts and the first version of the manuscript) validation of our model's forecast, confirming that the solar corona is currently in an active epoch with high probability for superflares. This fact underscores the necessity of continuous, multi-perspective monitoring of solar activity.

4.13. Limitations and Future Work

While the probabilistic spatiotemporal framework presented here offers a novel approach to forecasting S-class flares, several limitations must be acknowledged, and avenues for future improvements remain.

Limitations

1. *Model dependence on butterfly-diagram extrapolation*. Our spatial forecast relies on extending the sunspot-area butterfly diagram using a Monte Carlo approach based on historical patterns (Cycles 17–24). This assumes that the latitudinal migration and emergence patterns of Solar Cycles 25 and 26 will not deviate significantly from the past 150 years. However, should Cycle 25 exhibit unusual hemispheric asymmetry or a truncated/accelerated migration, the projected negative Laplacian bands (Figure 7b) may be displaced or less representative.
2. *Probabilistic*, *non-deterministic nature*. The framework identifies windows of enhanced probability, not individual events. Consequently, it cannot specify the exact timing, magnitude, or longitudinal origin of a given S-flare. This is an inherent limitation of any long-term probabilistic forecast and underscores that our product is a *risk map* rather than an event predictor.
3. *Potential for false positives and false negatives*. Historical validation (Cycles 17–24) shows that not every positive-phase window of the 1.7/7-year oscillations coincided with a recorded S-flare (though all S-flares fell within such windows). Similarly, our spatial filter (negative cross-Laplacian) may highlight zones where magnetic energy accumulates but is released through mechanisms other than S-class flares (e.g., sequential M/X-class flares, confined eruptions). The false-alarm rate and probability of detection can only be fully quantified after Cycle 25 concludes.
4. *Dependence on uniform GOES recalibration*. The S-flare catalog (1975–2024) relies on the recalibrated GOES SXR fluxes (Hudson et al., 2024). While this provides consistency, any residual systematic errors in early GOES measurements could affect the wavelet-derived periodicities and the morphology of the flare butterfly diagram.
5. *Lack of direct magnetic field inputs*. The current framework uses sunspot area and flare density as proxies for magnetic flux emergence and coronal energy release. It does not incorporate direct measurements of photospheric vector magnetic fields (e.g., from SDO/HMI) or coronal magnetic topology, which could refine the identification of energy-accumulation zones.

Table 5
Summary of Probabilistic Forecast Windows for S-Class Solar Flares (>X10) During Solar Cycles 25 and 26

Window	Solar Cycle	Time interval ± 0.2 years	Qualitative Probability	Preferred Latitudinal band	Figure 7 Coord.
1	25	2025.7–2026.6	High	05°S–20°S	A–a
1	25	2025.7–2026.6	Medium	20°S–25°S	A–a
1	25	2025.7–2026.6	High	10°N–25°N	A–a
1	25	2025.7–2026.6	Medium	05°N–10°N	A–a
2	25	2027.2–2027.9	Medium	05°S–15°S	B–b
2	25	2027.2–2027.9	Medium	05°N–10°N	B–b
3	25	2028.8–2029.7	Medium	05°S–15°S	C–c
3	25	2028.8–2029.7	Medium	05°N–10°N	C–c
4	26	2030.6–2031.5	High	10°S–15°S	D–d
4	26	2030.6–2031.5	Medium	05°N–20°N	D–d
5	26	2032.3–2033.2	Medium	05°S–15°S	E–e
5	26	2032.3–2033.2	High	10°N–20°N	E–e
6	26	2034.1–2034.9	High	05°S–15°S	F–f
6	26	2034.1–2034.9	High	10°N–20°N	F–f

Note. Qualitative probability is assigned based on the strength of the coupled-phase signal and the robustness of negative Laplacian structures in the projection. Spatiotemporal coordinates (e.g., A–a) refer to labels in Figure 7.

Future Work

1. *Integration with short-term forecasting models*. The identified high-risk windows (Table 5) should serve as a contextual prior for operational short-term flare-forecasting systems (e.g., machine-learning models using vector magnetograms). During windows A and B (2025–2027), space-weather agencies could trigger enhanced observational campaigns and increase the frequency of model updates.
2. *Assimilation of new observational data*. As Solar Cycle 25 progresses, the butterfly diagram and Laplacian maps should be updated in near-real time using data from GOES-18, Solar Orbiter, and Parker Solar Probe. This will allow dynamic adjustment of the forecasted latitudinal bands and improve the lead time for later windows (e.g., 2028–2029).
3. *Extension to other extreme space-weather phenomena*. The same coupled-oscillation model has already shown skill in retrospective forecasting of GLE events and intense geomagnetic storms. Future work should explicitly test its predictive capability for fast CMEs, solar energetic particle events, and geomagnetic indices (Dst, Kp) in a unified framework.
4. *Development of a real-time forecast verification platform*. A public dashboard could be established to track the progression of Solar Cycle 25 relative to the predicted high-probability windows and Laplacian bands. This would facilitate transparent validation and community feedback.
5. *Physical modeling of the 1.7-year and 7-year oscillations*. Our study identifies these two periodicities and their physical origins are tentatively proposed. The first oscillation is related to tachocline dynamics, magneto-Rossby waves, or coupled dynamo modes. The second oscillation remains unclear, but we speculate that it may arises from the beating (interference) between two magneto-Rossby modes with closely spaced periods (see the discussion under Section 4.8). Future theoretical work should aim to explain this oscillation within the solar dynamo theory, which could further constrain their stability and predictability over century timescales.

In summary, the proposed framework represents a significant step toward long-term probabilistic forecasting of extreme solar activity, but its ultimate utility will depend on continuous validation, integration with operational systems, and refinement through physical modeling. The ongoing Solar Cycle 25 provides a critical opportunity to test these predictions in real time and to refine the methodology for Cycle 26 and beyond.

4.14. A Scientific Reflection: Addressing Parker's 1963 Questions About Solar Flares Through Global Magnetic Diagnostics

Parker (1963) posed important questions about the nature of solar flares and explained the fundamental dilemma of solar flares. Sixty years later, while substantial progress has been made, Parker's questions remain unanswered at the global level. Solar flares pose a fundamental puzzle: the Sun stores vast amounts of magnetic energy in slowly evolving fields and releases it abruptly in a matter of minutes. After decades of observations, the essential difficulty remains–identifying where this energy is accumulated, how the magnetic field becomes primed for instability, and why eruptions occur only at particular moments.

As Parker (1963)) summarized: "the present state of the theory of solar-flare phenomenon ⋯ is to construct an energy source that can supply the 10^{32} ergs that seem to be expended by a large flare. The popular view at the present time [NB: even in 2025] is that this energy is released principally in the central portions of the visible flare. On the basis of this view it supposed that the energy arises from the annihilation of magnetic fields. We seem to find very little support for these ideas either in observation or in theory. ⋯ The observational and theoretical difficulties with the hypothesis of magnetic-field annihilation suggest that other alternatives for the flare must be explored."

Our analysis of nearly five decades of GOES SXR data introduces two global diagnostics that illuminate these questions from a new angle. The Laplacian of the SXR flare butterfly diagram ($\mathcal{L}_{\mathrm{SXR}}$), isolates regions of negative curvature as persistent sites of magnetic energy accumulation (Figure 5a). S-class flares cluster

preferentially within these zones, revealing that the buildup of free magnetic energy follows reproducible large-scale patterns rather than a random distribution across latitudes.

The second diagnostic, the cross-Laplacian ($\mathcal{L} = \mathcal{L}_{\text{spots}} * \mathcal{L}_{\text{SXR}}$), captures the degree of magnetic coherence vertically between the photospheric and coronal part of the solar atmosphere (Figure 5c). Extreme flares occur only where both layers simultaneously exhibit negative curvature. This alignment marks conditions in which magnetic stresses are coherently assembled across atmospheric heights, creating a vertically integrated reservoir of energy capable of catastrophic release. In this sense, the cross-Laplacian provides a quantitative measure of the breakdown in photosphere–corona coupling expected during major eruptions, and it reveals the global-scale restructuring that follows: a transition from negative to positive curvature after S-class events, signaling the dispersal of stored energy and a reorganization of magnetic topology. No non-magnetic mechanism seems necessary. The cross-Laplacian connects photospheric magnetic flux (sunspot area) with coronal energy release (SXR flares), demonstrating that the observed patterns emerge from the storage and sudden release of magnetic energy.

Temporal analysis adds an additional dimension. Wavelet methods show that S-class flares are modulated by the constructive interference of two global oscillations with periods near 1.7 and 7 years (Figure 6). These rhythms define windows in which the likelihood of magnetic instability is greatly enhanced. Local reconnection does not seemed to arise in isolation; it is conditioned by global dynamical states of the Sun. The appearance of S-class flares exclusively within these interference windows demonstrates that the probability of turbulence, or rapid topology change is governed by deep-seated dynamo oscillations rather than by purely local or stochastic processes.

The spatiotemporal clustering of extreme phenomena reinforces this picture. All 77 historical GLE events (1942–2025) and all major geomagnetic storms stronger than −250 nT fall within the same negative-curvature regions and the same phase windows that host S-class flares (Figure 7). Luminous flares, relativistic particle acceleration, and geoeffective CMEs thus emerge as different expressions of a single, globally orchestrated energy-release cycle. This coherence provides a natural explanation of energy partitioning channels: the visible flare is only one channel, not necessarily the dominant one, in a multi-component magnetic energy release process.

The relation between flare strength and underlying magnetic structures also becomes clearer. S-class flares correlate strongly with the largest sunspot groups (>1200 μHem), indicating that large-scale magnetic complexity sets the stage for extreme events. Small-scale braiding at ∼100 km may facilitate rapid reconnection, but it is the macroscopic non-potentiality seen in the butterfly diagram that determines where such microphysical processes can develop and manifest. The spatial forecasts that follow from this analysis identify specific high-probability latitudinal bands (e.g., 5°S–25°S during 2025.7–2026.6), enabling targeted observations to test whether favorable reconnection geometries–such as antiparallel field alignments–precede extreme events.

The clustering of GLE events, major geomagnetic storms, and S-class flares within the same negative-curvature domains indicates that these phenomena share a common energy reservoir. The system follows a three-stage cycle: (a) magnetic energy accumulates in regions of negative Laplacian; (b) constructive interference between the 1.7-year and 7-year oscillations raises the global probability of instability; (c) catastrophic release follows, manifested as flares, CMEs, and GLEs. This cycle operates across nested timescales: the 11-year dynamo modulates latitudinal drift, the 7-year mode sets broad activity envelopes, and the 1.7-year oscillation governs the triggering rhythm.

From this newly proposed framework, we obtain spatial forecasts with latitudinal precision of roughly 10° and temporal windows of about 1 year (Figure 7; Table 5). The highest-risk intervals for S-class flares in Solar Cycle 25 occur for time windows 2025.7–2026.6 and 2027.2–2027.9, with clear hemispheric preferences. This addresses the long-standing need for flare predictability based on physically motivated, global diagnostics.

Five decades of observations show that extreme flares are not isolated explosions but predictable outcomes of the Sun's global magnetic evolution. While the microphysics of fast reconnection remains an essential frontier, the global organization of magnetic fields–its storage, modulation, and release–acts as the framework within which those microphysical processes unfold.

As Solar Cycle 25 enters the predicted high-risk intervals, coordinated observations offer the possibility of capturing the transition from global magnetic accumulation states to sudden releases. Such observations will test

not only the specific forecasts presented here, but the broader idea that the Sun's most violent events arise from order rather than disorder; from a magnetic field whose evolution is structured, rhythmic, and occasionally compelled to break.

5. Conclusions

We have developed a probabilistic, physics-informed framework for forecasting S-class solar flares (>X10) based on nearly five decades (Solar Cycles 21–25) of GOES soft X-ray observations. The approach integrates morphological diagnostics of chromospheric-coronal activity with Bayesian inference to quantify spatial and temporal variations in solar flare probability.

1. *Probabilistic Nature of Forecasting*: S-flare forecasting is fundamentally probabilistic rather than deterministic. Our methodology identifies time-frequency zones of enhanced probability rather than predicting exact time or location occurrences, recognizing the inherent stochastic elements in solar eruptive processes.
2. *Hemispheric Asymmetry*: Our analysis confirms persistent hemispheric asymmetry in flare productivity, with southern hemisphere dominance established since solar cycle 22. This asymmetry is reflected in the gradient and Laplacian patterns of the butterfly diagram.
3. *Spatiotemporal Patterns*: The gradient and Laplacian of the chromospheric butterfly diagram provide powerful diagnostics for identifying regions susceptible to S-flare activity. S-flares consistently occur in the negative Laplacian regions, which likely correspond to zones of magnetic energy accumulation through reconnection processes.
4. *Cross-Laplacian*: This metric provides a powerful diagnostic of the non-linear interplay between magnetic-flux emergence in the photosphere and coronal energy release traced by SXR emission. Positive regions indicate coherent coupling and efficient transmission of magnetic stresses into the corona, whereas negative regions identify intervals of decoupling or independent evolution. The spatial and temporal organization of these structures across five solar cycles offers direct observational constraints on the vertical magnetic connectivity of the solar atmosphere and on the mechanisms linking the global dynamo to coronal heating.
5. *Temporal Modulation*: Wavelet analysis reveals that S-flare occurrence is co-modulated by two dominant periodicities: 1.7-year and 7-year oscillations. The 7-year periodicity amplitude-modulates the shorter 1.7-year cycle, with S-flares occurring preferentially during constructive interference phases.
6. *Cycles 25 and 26 Forecasts*: Based on the phase relationship of these oscillations, we identify 2025.7 ± 0.2–2026.6 ± 0.2, 2027.2 ± 0.2–2027.9 ± 0.2, and 2028.8 ± 0.2–2029.7 ± 0.2 years as three high-probability windows for S-flare occurrence during Solar Cycle 25, and during 2030.6–2031.5, 2032.3–2033.2, and 2034.1–2034.9 in Cycle 26. This forecast is consistent with the expected equatorward migration of magnetic activity and the development of negative Laplacian regions during this period.
7. *Operational Implications*: The probabilistic framework developed here provides advance warning of heightened risk periods for extreme space weather, enabling improved preparedness for potential impacts on technological systems. This approach complements traditional point-forecasting methods by focusing on risk assessment rather than deterministic predictions.

These series of findings enhance our understanding of solar magnetic field evolution and provide observational constraints for models of flare productivity and magnetic energy accumulation and release processes. The continued monitoring of the development of Solar Cycle 25 and beyond will provide crucial data for understanding the long-term evolution of these patterns.

Conflict of Interest

The authors declare no conflicts of interest relevant to this study.

Data Availability Statement

Catalogs of GOES SXR flares

1. Reuven Ramaty High Energy Solar Spectroscopic Imager, NASA [Data set]. https://hesperia.gsfc.nasa.gov/goes/.

2. NGDC [Data set].
   https://www.ngdc.noaa.gov/stp/space-weather/solar-data/solar-features/.
3. World Data Center for Solar-Terrestrial Physics [Data set].
   http://www.wdcb.ru/stp/solar/.
4. Archival Solar Flares Catalog.

- Hudson, H., Cliver, E., White, S. et al. (2024) [Data set] The Greatest GOES SXR Flares: Saturation and Recalibration over Two Hale Cycles. Solar Physics, 299, 39. https://doi.org/10.1007/s11207-024-02287-x.
- Berretti et al. (2025) [Data set] Asr: Archival solar flares catalog. The Astrophysical Journal Supplement Series, 278 (1), 9. https://doi.org/10.3847/1538-4365/adc731.
- Janssens et al. (2025) [Data set] Solar flare rates and probabilities based on the McIntosh classification: Impacts of GOES/XRS rescaling and revisited sunspot classifications. J. Space Weather Space Clim., 15 (14). https://doi.org/10.1051/swsc/2025007.
- Tan et al. (2025) [Data set] The Occurrence of Powerful Flares Stronger than X10 Class in Solar Cycles. ApJL, 979, L16. https://doi.org/10.3847/2041-8213/ada611.

Solar Activity Indices

5. hSFI:

- Velasco Herrera et al., 2025, "Solar flare activity, 1937–2024: Introducing the new hSFI in the context of 2024's major solar storm events (Northern Hemisphere)", [Data set]. https://doi.org/10.7910/DVN/TSQEPB, Harvard Dataverse, V4.
- Velasco Herrera et al., 2025, "Solar flare activity, 1937–2024: Introducing the new hSFI in the context of 2024's major solar storm events (South Hemisphere)", [Data set]. https://doi.org/10.7910/DVN/C1L8ZX, Harvard Dataverse, V4.

6. The dates of the GLEs events [Data set].
   https://www.ngdc.noaa.gov/stp/space-weather/interplanetary-data/.
   https://www.nmdb.eu/nest/.
7. The daily sunspot area (Royal Greenwich Observatory and USAF/NOAA) [Data set].
   http://solarcyclescience.com/activeregions.html.

Wavelet Analysis

Torrence & Compo. (1998). "A Practical Guide to Wavelet Analysis", [Software] https://paos.colorado.edu/research/wavelets/.

Acknowledgments
This research was facilitated by multiple international collaborations. We would like to thank both referees for their constructive suggestions for the improvement of the manuscript. We acknowledge the use of GOES SXR flare data from NOAA. Willie Soon would like to thank Dr. Ronan Connolly and Dr. Laszlo Szarka for their intellectual supports and encouragements. V.M. Velasco Herrera acknowledges the support of PAPIIT-IT101126 "Pronóstico de Eventos Solares Extremos Mediante Inteligencia Artificial." G. Velasco Herrera acknowledges the support of PAPIME-PE112226 and Collaboration Guidelines No. DGAJ-PDI-200623-1262. V.M. Velasco Herrera thanks the Eksperimental'naya Laboratoriya iSkusstvennogo intellektY (ELSY).

References

Bai, T. (1987). Distribution of flares on the sun: Superactive regions and active zones of 1980–1985. *The Astrophysical Journal*, *314*, 795–807. https://doi.org/10.1086/165105
Bai, T., & Sturrock, P. A. (1989). Classification of solar flares. *ARA*, *27*(1), 421–467. https://doi.org/10.1146/annurev.aa.27.090189.002225
Bathe, K.-J. (1996). *Finite element procedures*. Prentice Hall.
Beck, J. G. (2000). A comparison of differential rotation measurements. *Solar Physics*, *191*(1), 47–70. https://doi.org/10.1023/a:1005226402796
Benevolenskaya, E. E. (1995). Double magnetic cycle of the solar activityl. *Solar Physics*, *161*, 1–8. https://doi.org/10.1007/bf00732080
Benevolenskaya, E. E. (1996). A model of the double magnetic cycle of the sun. *ApJ*, *509*(1), L49–L52. https://doi.org/10.1086/311755
Berdyugina, S. V., & Usoskin, I. G. (2003). Active longitudes in sunspot activity: Century scale persistence. *A&A*, *405*(3), 1121–1128. https://doi.org/10.1051/0004-6361:20030748
Berretti, M., Mestici, S., Giovannelli, L., Del Moro, D., Stangalini, M., Giannattasio, F., & Berrilli, F. (2025). Asr: Archival solar flares catalog. *The Astrophysical Journal - Supplement Series*, *278*(1), 9. https://doi.org/10.3847/1538-4365/adc731
Bloomfield, D. S., Higgins, P. A., McAteer, R. T. J., & Gallagher, P. T. (2012). Toward reliable benchmarking of solar flare forecasting methods. *The Astrophysical Journal Letters*, *747*(2), L41. https://doi.org/10.1088/2041-8205/747/2/L41
Bobra, M. G., & Couvidat, S. (2014). Solar flare prediction using SDO/HMI vector magnetic field data with a machine-learning algorithm. *ApJ*, *798*(2), 135. https://doi.org/10.1088/0004-637X/798/2/135
Bobra, M. G., & Couvidat, S. (2015). Solar flare prediction using sdo/hmi vector magnetic field data with a machine-learning algorithm. *The Astrophysical Journal*, *798*(2), 135. https://doi.org/10.1088/0004-637X/798/2/135
Camporeale, E., & Berger, T. E. (2025). Verification of the NOAA space weather prediction center solar flare forecast (1998-2024). *Space Weather*, *23*(10), e2024SW004123. https://doi.org/10.1029/2025SW004546
Carrington, R. C. (1858). On the distribution of the solar spots in latitudes since the beginning of the year 1854; with a map. *Monthly Notices of the Royal Astronomical Society*, *19*(1), 1–3. https://doi.org/10.1093/mnras/19.1.1a
Charbonneau, P. (2020). Dynamo models of the solar cycle. *Living Reviews in Solar Physics*, *17*(1), 4. https://doi.org/10.1007/s41116-020-00025-6

Cliver, E. W., Schrijver, C. J., Shibata, K., & Usoskin, I. G. (2022). Extreme solar events. *Living Reviews in Solar Physics*, *19*(1), 2. https://doi.org/10.1007/s41116-022-00033-8

Deng, L. H., Gai, N., Tang, Y. K., Xu, C. L., & Huang, W. J. (2013a). Phase asynchrony of hemispheric flare activity revisited: Empirical mode decomposition and wavelet transform analyzes. *Astrophysics and Space Science*, *343*(1), 27–32. https://doi.org/10.1007/s10509-012-1231-2

Deng, L. H., Qu, Z. Q., Liu, T., & Wang, K. R. (2013b). The hemispheric variation of the flare index during solar cycles 20–23. *Astronomische Nachrichten*, *334*(3), 217–222. https://doi.org/10.1002/asna.201111786

Deng, L. H., Zhang, X. J., Li, G. Y., Deng, H., & Wang, F. (2019). Phase and amplitude asymmetry in the quasi-biennial oscillation of solar Hα flare activity. *Monthly Notices of the Royal Astronomical Society*, *488*(1), 111–119. https://doi.org/10.1093/mnras/stz1653

Dhakal, S. K., & Zhang, J. (2023). What are the causes of super activity of solar active regions? *The Astrophysical Journal*, *960*(1), 36. https://doi.org/10.3847/1538-4357/ad07d2

Dikpati, M., & McIntosh, S. W. (2020). Space weather challenge and forecasting implications of rossby waves. *Space Weather*, *18*(3), e2018SW002109. https://doi.org/10.1029/2018SW002109

Feynman, J. (1982). Geomagnetic and solar wind cycles, 1900–1975. *Journal of Geophysical Research*, *87*(A8), 6153–6162. https://doi.org/10.1029/JA087iA08p06153

Gailitis, A., Gerbeth, G., Gundrum, T., Lielausis, O., Lipsbergs, G., Platacis, E., & Stefani, F. (2018). Self-excitation in a helical liquid metal flow: The Riga dynamo experiments. *Journal of Plasma Physics*, *84*(3), 735840301. https://doi.org/10.1017/S0022377818000363

Gilman, D. L., Fuglister, E. J., & Mitchell, J. R. (1963). On the power spectrums of "red noise". *Journal of the Atmospheric Sciences*, *20*, 182–190.

Gyenge, N., Ludmány, A., & Baranyi, T. (2016). Active longitudes and solar flares ocurrences. *Apj*, *818*, 127. https://doi.org/10.3847/0004-637X/818/2/127

Hathaway, D. H., & Upton, L. (2014). The solar meridional circulation and sunspot cycle variability. *Journal of Geophysical Research: Space Physics*, *119*(5), 3316–3324. https://doi.org/10.1002/2013ja019432

Hayakawa, H., Bechet, S., Clette, F., Hudson, H. S., Maehara, H., Namekata, K., & Notsu, Y. (2023). Magnitude estimates for the carrington flare in 1859 September: As seen from the original records. *The Astrophysical Journal Letters*, *954*(1), L3. https://doi.org/10.3847/2041-8213/acd853

Huang, G., Duan, G., Wan, M., Zhao, X., Xu, T., Deng, L., et al. (2025). Quasiperiodic variations of the goes soft x-ray flares during solar cycles 21–25. *ApJ*, *280*(2), 60. https://doi.org/10.3847/1538-4365/ae0033

Hudson, H. S., Cliver, E., White, S., Machol, J., Peck, C., Tolbert, K., et al. (2024). The greatest GOES soft X-ray flares: Saturation and recalibration over two hale cycles. *Solar Physics*, *299*(3), 39. https://doi.org/10.1007/s11207-024-02287-x

Hughes, T. J. R. (2000). *The finite element method: Linear static and dynamic finite element analysis*. Dover Publications.

Janssens, J., Delouille, V., Clette, F., & Andries, J. (2025). Solar flare rates and probabilities based on the mcintosh classification: Impacts of goes/xrs rescaling and revisited sunspot classifications. *Journal of Space Weather and Space Climate*, *15*(14), 14. https://doi.org/10.1051/swsc/2025007

Jing, J., Tan, C., Yuan, Y., Wang, B., Wiegelmann, T., Xu, Y., & Wang, H. (2010). Free magnetic energy and flare productivity of active regions. *The Astrophysical Journal*, *713*(1), 440–449. https://doi.org/10.1088/0004-637X/713/1/440

Kane, R. P. (2002). Variability in the periodicity of 27 days in solar indices. *Solar Physics*, *209*(1), 207–218. https://doi.org/10.1023/a:1020959817176

Kontogiannis, I., Zhu, Y., Barczynski, K., Stiefel, M. Z., Collier, H., McKevitt, J., et al. (2025). Near-continuous tracking of solar active region noaa 13664 over three solar rotations. *Astronomy and Astrophysics*, *704*, A105. https://doi.org/10.1051/0004-6361/202556136

Korsós, M. B., Dikpati, M., Erdélyi, R., Liu, J., & Zuccarello, F. (2023). On the connection between rieger-type and magneto-rossby waves driving the frequency of the large solar eruptions during solar cycles 19–25. *The Astrophysical Journal*, *944*(2), 180. https://doi.org/10.3847/1538-4357/acb64f

Korsós, M. B., & Erdélyi, R. (2025). Where do solar storms prefer to originate from: Hemispheric and longitudinal patterns in solar cycles 23 and 24. *The Astrophysical Journal*, *989*(2), 162. https://doi.org/10.3847/1538-4357/adee97

Le, G. M., & Liu, G. A. (2020). The properties of source locations and solar cycle distribution of gles during 1942–2017. *Solar Physics*, *295*(35), 35. https://doi.org/10.1007/s11207-020-01600-8

Leamon, R. J., McIntosh, S. W., & Title, A. (2022). Deciphering solar magnetic activity: The solar cycle clock. *Frontiers in Astronomy and Space Sciences*, *9*, 886670. https://doi.org/10.3389/fspas.2022.886670

Leka, K. D., Park, S.-H., Kusano, K., Andries, J., Barnes, G., Bingham, S., et al. (2019). A comparison of flare forecasting methods. III. Systematic behaviors of operational solar flare forecasting systems. *ApJ*, *881*(2), 101. https://doi.org/10.3847/1538-4357/ab2e11

Li, Q., Zhang, X.-W., & Le, G.-M. (2024). Latitudinal and solar cycle distribution of extreme (≥x5) flares during 1976–2018. *Research in Astronomy and Astrophysics*, *24*(12), 125007. https://doi.org/10.1088/1674-4527/ad90b0

Lin, J., Wang, F., Deng, L., Deng, H., Mei, Y., & Zhang, X. (2023). Evolutionary relationship between sunspot groups and soft x-ray flares over solar cycles 21–25. *The Astrophysical Journal*, *958*(1), 1. https://doi.org/10.3847/1538-4357/ad0469

Maunder, E. W. (1904). Note on the distribution of sun-spots in heliographic latitude, 1874-1902. *Monthly Notices of the Royal Astronomical Society*, *64*(8), 747–761. https://doi.org/10.1093/mnras/64.8.747

McIntosh, S. W., Leamon, R. J., Krista, L. D., Title, A. M., Hudson, H. S., Riley, P., et al. (2015). The solar magnetic activity band interaction and instabilities that shape quasi-periodic variability. *Nature Communications*, *6*(1), 6491. https://doi.org/10.1038/ncomms7491

McIntosh, S. W., Wang, X., Leamon, R. J., Davey, A. R., Howe, R., Krista, L. D., et al. (2014). Deciphering solar magnetic activity. I. On the relationship between the sunspot cycle and the evolution of small magnetic features. *ApJ*, *792*(1), 12. https://doi.org/10.1088/0004-637X/792/1/12

Mendoza, B., Velasco, V. M., & Valdés-Galicia, J. (2006). Mid-term periodicities in the solar magnetic flux. *Solar Physics*, *233*(2), 319–330. https://doi.org/10.1007/s11207-006-4122-2

Mendoza, B., & Velasco Herrera, V. M. (2011). On mid-term periodicities in sunspot groups and flare index. *Solar Physics*, *271*(1), 169–182.

Miroshnichenko, L. (2015). *Solar cosmic rays*. Springer. https://doi.org/10.1007/978-3-319-09429-8

Miroshnichenko, L. I., Perez-Peraza, J. A., Velasco-Herrera, V. M., Zapotitla, J., & Vashenyuk, E. V. (2012). Oscillations of galactic cosmic rays and solar indexes before arrival of relativistic protons from the sun. *Geomagnetism and Aeronomy*, *52*(5), 547–560. https://doi.org/10.1134/S001679321205012X

Moss, D. (1999). Non-axisymmetric solar dynamos. *MNRAS*, *306*(2), 300–306. https://doi.org/10.1046/j.1365-8711.1999.02510.x

Nandy, D. (2006). Magnetic helicity and flux tube dynamics in the solar convection zone: Comparisons between observation and theory. *Journal of Geophysical Research*, *111*(A12), A12S01. https://doi.org/10.1029/2006ja011882

Norton, A., Howe, R., Upton, L., & Usoskin, I. (2023). Solar cycle observations. *Space Science Reviews*, *219*(64), 64. https://doi.org/10.1007/s11214-023-01008-3

Parker, E. N. (1955). The formation of sunspots from the solar toroidal field. *The Astrophysical Journal*, *121*, 491. https://doi.org/10.1086/146010
Parker, E. N. (1963). The solar-flare phenomenon and the theory of reconnection and annihilation of magnetic fields. *The Astrophysical Journal - Supplement Series*, *8*, 177–212. https://doi.org/10.1086/190087
Pontin, D., & Priest, E. (2022). Magnetic reconnection: Mhd theory and modelling. *Living Reviews in Solar Physics*, *19*(1), 1. https://doi.org/10.1007/s41116-022-00032-9
Prasad, A., Roy, S., Ghosh, K., Panja, S. C., & Patra, S. N. (2021). Investigation of hemispherical variations of soft x-ray solar flares during solar cycles 21 to 24. *Solar System Research*, *55*(2), 169–182. https://doi.org/10.1134/s0038094621020052
Prasad, A., Roy, S., Panja, S. C., & Patra, S. N. (2022). Study of distribution and asymmetry in soft x-ray flares over solar cycles 21-24. *Geomagnetism and Aeronomy*, *62*(3), 286–304. https://doi.org/10.1134/S0016793222030033
Rossby, C.-G. (1939). Relation between variations in the intensity of the zonal circulation of the atmosphere and the displacements of the semi-permanent centers of action. *Journal of Marine Research*, *2*(1), 38–55. https://doi.org/10.1357/002224039806649023
Schwabe, H., & Schwabe, H. (1844). Sonnen-beobachtungen im jahre 1843. *Astronomische Nachrichten*, *21*(15), 233–235. https://doi.org/10.1002/asna.18440211505
Singh, A., Chaudhari, A., Sharma, G., & Singh, A. K. (2024). Variation in the flaring potential of different sunspot groups during different phases of solar cycles 23 and 24. *Research in Astronomy and Astrophysics*, *24*(2), 025012. https://doi.org/10.1088/1674-4527/ad1922
Soon, W., Velasco Herrera, V. M., Cionco, R. G., Qiu, S., Baliunas, S., Egeland, R., et al. (2018). Covariations of chromospheric and photometric variability of the young sun analogue hd 30495: Evidence for and interpretation of mid-term periodicities. *Monthly Notices of the Royal Astronomical Society*, *483*(2), 2748–2757. https://doi.org/10.1093/mnras/sty3290
Stefani, F., Horstmann, G. M., Mamatsashvili, G., Weber, N., Rädler, K.-H., Jouve, L., & Arlt, R. (2025). Adding further pieces to the synchronization puzzle: Qbo, bimodality, and phase jumps. *Solar Physics*, *300*(8), 110. https://doi.org/10.1007/s11207-025-02521-0
Stiefel, M. Z., Kuhar, M., Limousin, O., Dickson, E. C. M., Volpara, A., Hurford, G. J., & Krucker, S. (2025). Using the stix background detector as a proxy for goes. *Astronomy and Astrophysics*, *694*, A138. https://doi.org/10.1051/0004-6361/202452574
Suykens, J. A. K., Van Gestel, T., De Brabanter, J., De Moor, B., & Vandewalle, J. (2005). *Least squares support vector machines*. World Scientific.
Tan, B., Zhang, Y., Huang, J., & Ji, K. (2025). The occurrence of powerful flares stronger than X10 class in solar cycles. *ApJL*, *979*(1), L16. https://doi.org/10.3847/2041-8213/ada611
Tian, L., Liu, Y., & Wang, J. (2002). The Most violent super-active regions in the 22nd and 23rd cycles. *Solar Physics*, *209*(2), 361–374. https://doi.org/10.1023/A:1021270202680
Toriumi, S., & Wang, H. (2019). Flare-productive active regions. *Living Reviews in Solar Physics*, *16*(1), 3. https://doi.org/10.1007/s41116-019-0019-7
Torrence, C., & Compo, G. P. (1998). A practical guide to wavelet analysis. *Bulletin of the American Meteorological Society*, *79*, 61–78. https://doi.org/10.1175/1520-0477(1998)079⟨0061:APGTWA⟩2.0.CO;2
Velasco Herrera, V., Soon, W., Knoska, S., Özgüç, A., Velasco Herrera, G., Yeşilyaprak, H., et al. (2025). Solar flare activity, 1937-2024: Introducing the new hemispheric solar flare index (hsfi) in the context of 2024's major solar storm events. *Space Weather*, *23*(11), e2025SW004515. https://doi.org/10.1029/2025SW004515
Velasco Herrera, V., Soon, W., & Legates, D. (2021). Does machine learning reconstruct missing sunspots and forecast a new solar minimum? *Advances in Space Research*, *68*(3), 1485–1501. https://doi.org/10.1016/j.asr.2021.03.023
Velasco Herrera, V. M., Perez-Peraza, J., Soon, W., & Marquez-Adame, J. C. (2018). The quasi-biennial oscillation of 1.7 years in ground level enhancement events. *New Astronomy*, *60*, 7–13. https://doi.org/10.1016/j.newast.2017.09.007
Vernazza, J. E., Avrett, E. H., & Loeser, R. (1981). Structure of the solar chromosphere. Iii. Models of the euv brightness components of the quiet sun. *The Astrophysical Journal - Supplement Series*, *45*, 635–725. https://doi.org/10.1086/190731
Woods, T. N., Eden, T., Eparvier, F. G., Jones, A. R., Woodraska, D. L., Chamberlin, P. C., & Machol, J. L. (2024). GOES-R series X-ray sensor (XRS): 1. design and pre-flight calibration. *Journal of Geophysical Research: Space Physics*, *129*(e2024JA032925), e2024JA032925. https://doi.org/10.1029/2024JA032925
Xiong, B., Wang, T., Li, X., & Yin, Y. (2021). Statistical analysis of soft x-ray solar flares during solar cycles 22, 23, and 24. *Astrophysics and Space Science*, *366*(1), 1. https://doi.org/10.1007/s10509-020-03909-z
Xu, D., Sun, P., Feng, S., Liang, B., & Dai, W. (2025). Solar flare forecasting using hybrid neural networks. *The Astrophysical Journal - Supplement Series*, *276*(2), 68. https://doi.org/10.3847/1538-4365/ada281
Zaqarashvili, T. V., Oliver, R., Ballester, J. L., & Shergelashvili, B. M. (2007). Rossby waves in "shallow water" magnetohydrodynamics. *Astronomy and Astrophysics*, *470*(3), 815–820. https://doi.org/10.1051/0004-6361:20077382
Zienkiewicz, O. C., Taylor, R. L., & Zhu, J. Z. (2005). *The finite element method: Its basis and fundamentals* (6th ed.). Butterworth-Heinemann.